**The Pennsylvania State University**

**The Graduate School**

**Department of Aerospace Engineering**

# CONCEPTUAL DEVELOPMENT OF CASING PATTERNS TO REDUCE THE AERODYNAMIC LOSSES IN AN AXIAL TURBINE STAGE

A Thesis in

Aerospace Engineering

by

Amrat Arvind Ranka



Submitted in Partial Fulfillment
of the Requirements
for the Degree of

Master of Science

December 2019

The thesis of Amrat Arvind Ranka was reviewed and approved* by the following:

Cengiz Camci
Professor of Aerospace Engineering
Thesis Advisor

Sven Schmitz
Associate Professor of Aerospace Engineering

Amy R. Pritchett
Professor of Aerospace Engineering
Head of the Department, Aerospace Engineering

*Signatures are on file in the Graduate School

# ABSTRACT

In turbomachinery, the presence of gap between the rotor blade tip and the casing surface has been a significant source of aerodynamic loss in the turbine flow field. This thesis seeks to understand and mitigate the aerodynamic losses by embedding different groove patterns on the casing surface near the turbine blade tip. A similar approach has been used in the past for the compressor stage to improve its stall and surge characteristics. However, extensive studies have not been performed for the turbine stage. Three different casing designs, "Spherical Patterns", "Axial Grooves", "Circumferential Grooves", were analyzed, and their effectiveness was measured against the smooth casing surface (baseline design). Based on the understanding of the preliminary casing designs, an improved casing design was developed. This thesis describes a comprehensive computational flow visualization study and aerodynamic experiments conducted at the Axial Flow Turbine Research Facility (AFTRF). Steady-state computational simulations were performed by solving three-dimensional Reynolds-Averaged-Navier-Stokes (RANS) flow equations. To accurately predict the flow near the tip section, including flow leaking through the tip gap, the Shear Stress Transport (SST) $k-\omega$ turbulence model with gamma-transition is employed. At first, the computational results were validated against the experimental results obtained for the preliminary casing designs. Furthermore, numerical studies were performed for different casing patterns to understand the flow physics and analyze the changes caused by such casing patterns in the turbine stage. With the aid of 3-D flow visualization plots, tip leakage losses and vortex structures of all designs were analyzed. Along with these plots, numerical calculations were employed to quantify the aerodynamic performance of different designs.

# TABLE OF CONTENTS

## LIST OF FIGURES

# List of Tables

# Nomenclature

| | |
|---|---|
| c | Midspan Axial Chord Length of Nozzle Guide Vane, m |
| $C_P$ | Total Pressure Coefficient; $\left(P_o - P_{o1_{avg}}\right)/ (0.5\rho U_m^2)$ |
| $C_p'$ | Rotor Static Pressure Coefficient; $\left(p - p_{3avg}\right)/ (0.5\rho_2 W_{x2,avg}^2)$ |
| $C_p$ | Nozzle Static Pressure Coefficient; $(p - P_{01_{avg}})/ (0.5\rho W_{x1,avg}^2)$ |
| p | Static Pressure, Pa |
| $P_0$ | Absolute Total Pressure, Pa |
| $T_0$ | Total Temperature, K |
| $U_m$ | Blade Speed at Mean Radius, m/s |
| $V$ | Velocity Magnitude, m/s |
| $V_x$ | Axial Velocity Component, m/s |
| $V_r$ | Radial Velocity Component, m/s |
| $V_\theta$ | Tangential Velocity Component, m/s |
| $W_{x,avg}$ | Average Axial Velocity, m/s |
| $y^+$ | Non-Dimensional Wall Coordinate |

**Subscript**

| | |
|---|---|
| 1 | Nozzle Guide Vane Inlet |
| 2 | Nozzle Guide Vane Exit or Rotor Inlet (Mixing Plane Interface) |
| 3 | Rotor Exit |

**Acronyms**

| | |
|---|---|
| AFTRF | Axial Flow Turbine Research Facility |
| CFD | Computational Fluid Dynamics |
| CCW | Counterclockwise |
| CW | Clockwise |
| FOM | Figure of Merit |
| HHV | Hub side Horseshoe Vortex |
| HP | High Pressure |
| HPV | Hub Passage Vortex |
| LP | Low Pressure |
| LV | Leakage Vortex |
| NGV | Nozzle Guide Vanes |
| PS | Pressure Side |
| PS-HV | Pressure side leg of Horseshoe Vortex |
| RANS | Reynolds Averaged Navier Stokes |
| SS | Suction Side |
| SS-HV | Suction side leg of Horseshoe Vortex |
| SST | Shear Stress Transport |
| THV | Tip side Horseshoe Vortex |
| TKE | Turbulent Kinetic Energy |
| TPV | Tip Passage Vortex |

# ACKNOWLEDGMENTS

This thesis became possible due to many people who supported me in my master's journey. I would like to thank all of them who helped me directly or indirectly in this journey.

First of all, a loud shout of thanks to my advisor Dr. Cengiz Camci. He is the most patient and understanding professor I ever met. He was always kind and guided me constantly in this process. This thesis became possible because of his efforts and support. Thank you, Dr. Schmitz, for agreeing to read my thesis in a short time span. I would also like to thank the Department of Aerospace Engineering for providing me the support in the form of teaching assistantship. Thanks to Dr. Pritchett for supporting me on this journey. The entire department staff was always cheerful, kind and helpful.

Prof. Rick and Ann are awesome. They are the best couple. Sunday's church sessions and alpha sessions with you all was really enjoying. And thanks to Ann for amazing food! Prof. Rick is a great mentor and was always there for me if I needed any help. He did so much for me that I don't know how to express that in words. The best part was working with Keith and JD in the summer. They are kind, joyful and understanding. I was able to learn so many things from them, which I am pretty sure would be very helpful in my future. Prof. Keith always used to scare me, but he treated me like his son :)

Thanks to my lab colleagues Veerandra, Gohar Mitansh and Aravinth, who helped me a lot in my thesis. I learned a lot from them as they were truly experts in this field. At Penn State, I was fortunate to have so many good best friends. They are the major chunk of my time at Penn State. Life at Penn State would have been so boring without you all. Thank you, Amit bhai for being a kind friend and never getting annoying. Thanks, Karthik for always mentoring me and teaching me many things. You are too smart! Venkatji, Sujay and Snehal were always there for me. Thanks, Venkatji and Mitansh for proof-reading this thesis. Special thanks to Snehal for cooking awesome food always. Thank you Priyesh and Radhika for being kindest neighbor and Swapnil for lunchtime fun. Thank you, Akhil for being the kind and sweet friend. I am very grateful to share the joyful moments with Dohwan and Thao. And yeah Mitansh, a friend like you made my life so simple out here. I guess a million thanks would also be less for your friendship.

My friends and people out here became like a family. Although, my real family was across the seven seas in India, but they are the reason for where I stand now. My dad and mom always kept me motivated and they are the reason for my smile. I am thankful to my awesome brother. I was able to go through all the huge tasks because of his good wishes. I would also like to thank my friends from undergrad, Kaushal, Aditi and Devashri. Your support and concern for me is always appreciated. Most importantly, I thank you God for being with me always.

# Chapter 1

## Introduction

Gas turbines have become a great source of power generation in the fields of aviation and industrial power generation. A gas turbine acts as a device that transfers energy to or from a moving fluid by the action of moving blades. The gas turbine industry has evolved in many ways from the past few decades. They are an essential component in many aerospace vehicles, marine vehicles, land vehicles, energy and industrial applications [1]. In addition, miniature versions of gas turbines, known as Microturbines, have found applications as auxiliary power units (APU) and as small jet engines for aero-propulsion tasks. Because of the wide range of applications, improving its efficiency has an enormous impact on these applications.

Gas turbines can be categorized as axial-flow, radial-flow and mixed flow turbines depending on the fluid flow direction. Based on the current experimental facility, the focus was kept on the axial flow gas turbine which is used typically in a high-pressure stage. In an axial turbine meridional fluid flow path is predominantly parallel to the inlet axis. The schematic of a conventional axial flow gas turbine is shown in Figure 1-1.

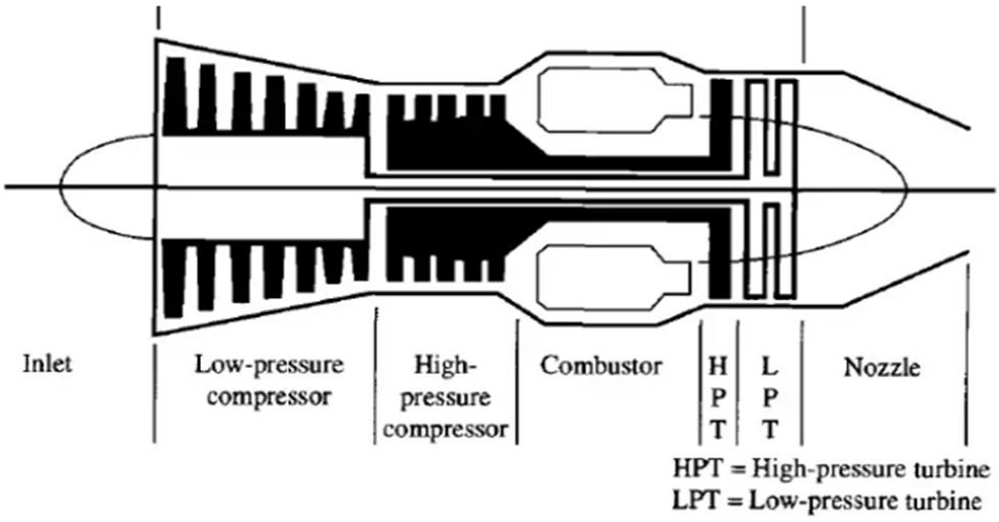


Figure 1-1 Schematic of Axial Flow Gas Turbine [2]

As seen from the schematic in Figure 1-1, gas turbines involve numerous components. Researchers in the aero-propulsion and turbomachinery industry are working to improve the performance of individual strategical parts such as intake baffle, compressor, combustor, gearbox, turbine and exhaust systems. Different fluid (leakage losses), thermal (tip-cooling), structural (high strength materials), vibrations (dynamic balancing) and systems (fuel injection rate) related research areas are being explored to improve the overall performance. In an effort towards efficiency improvement in turbines, this research study emphasizes on the fluid dynamics aspect of the turbine stage in an axial gas turbine. Before discussing the objectives and structure of the thesis, it is a good practice to understand the complex flow features and leakage losses present in a turbine stage.

### 1.1 Turbine Flow Field

The turbine flow field involves one of the most complex flow features. The presence of blades, crossflows and vortex formations create complexities in the analysis of this aero-thermal system (turbine). The flow arriving from the combustor outlet initially passes through the stationary Nozzle Guide Vanes (NGV), which forms the stator section of the HP turbine stage. Further, the fluid is directed through the rotating rotor section of the turbine. Flow fields in the nozzle and rotor section field involve viscous and inviscid flow regions. The core flow, which is approximately between two subsequent blades, can be treated as inviscid flow. The flow passing near the blade, hub surface and the casing surface, experiences viscous effects in the boundary layers. Research presented in this thesis specifically focuses on the rotor flow field as all design modifications are made in the rotor section.

Typically, turbine losses in the rotor are classified as profile losses, endwall secondary flow losses and tip leakage losses. Profile losses are usually attributed to the strong viscous interactions in the passage flow. Boundary layer formation around the blade surface is the major source of profile

losses. Generally, profile losses include blade wake and losses due to blade surface. Secondary and leakage losses are generated because of the presence of endwalls. The three-dimensional flow characteristics in the turbine passage cannot be completely understood without the presence of the secondary flows. The secondary flow developed due to boundary layer interactions in the turbine passage is the major reason for its efficiency reduction. The secondary flows are the result of turning of the vorticity vector. This complex phenomenon can be explained using vortical structures formations shown in Figure 1-2. The vortical structures are known as three-dimensional vortices which rotates around an axis line. Due to the airfoil shape of the turbine blade, the pressure around the pressure side and suction side of the turbine blade is not the same. This pressure difference results in vortices formation known as the Passage Vortex (PV). The vortical structures are also created in turbines due to flow around the boundary surface of the hub endwall and casing surface. The boundary layer interactions between the end wall and blade surface lead to complex secondary flows in the passage like the Horse-Shoe Vortex (HV). Further losses due to the Leakage Vortex (LV) is the result of flow leaking through the tip gap of the blades. All these flow vortices are discussed in further sections in detail.

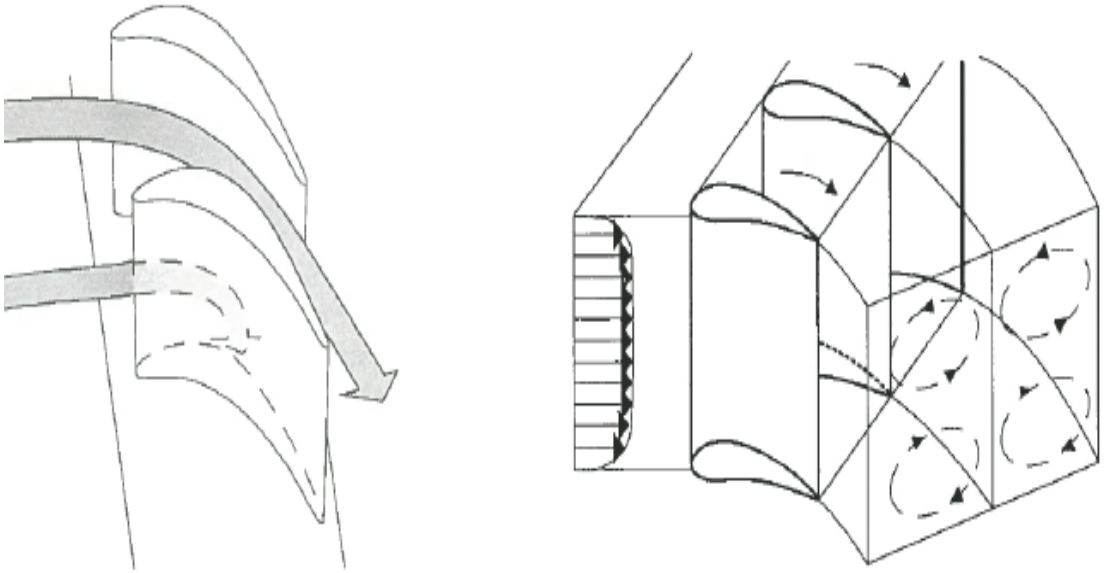

Figure 1-2 Cross-Stream Free Flow (left) and Fluid Endwall Boundary Layer (right) [5]

### 1.1.1 Horse-Shoe Vortex

Langston [3] and Sharma and Butler [4] explained that, due to both endwalls, there is the generation of a Horseshoe Vortex (HV). This HV develops when the boundary layer fluid on the casing or hub surface interacts with the leading edge of the turbine blade. The blade leading edge splits the flow into two parts, as shown on the left side of Figure 1-3. One part of the flow turns towards the suction side and is known as the Suction Side leg of the Horseshoe Vortex (SS-HV). The other part of the flow turns towards the pressure side and is known as the Pressure Side leg of the Horseshoe Vortex (PS-HV). As the flow moves from the leading edge to the trailing edge of the blade, PS-HV moves towards the SS of the blade and the outer casing. The SS-HV rotates in a counter-clockwise direction (CCW). Both PS-HV and SS-HV vortex counteract each other as shown in Figure 1-3 below.

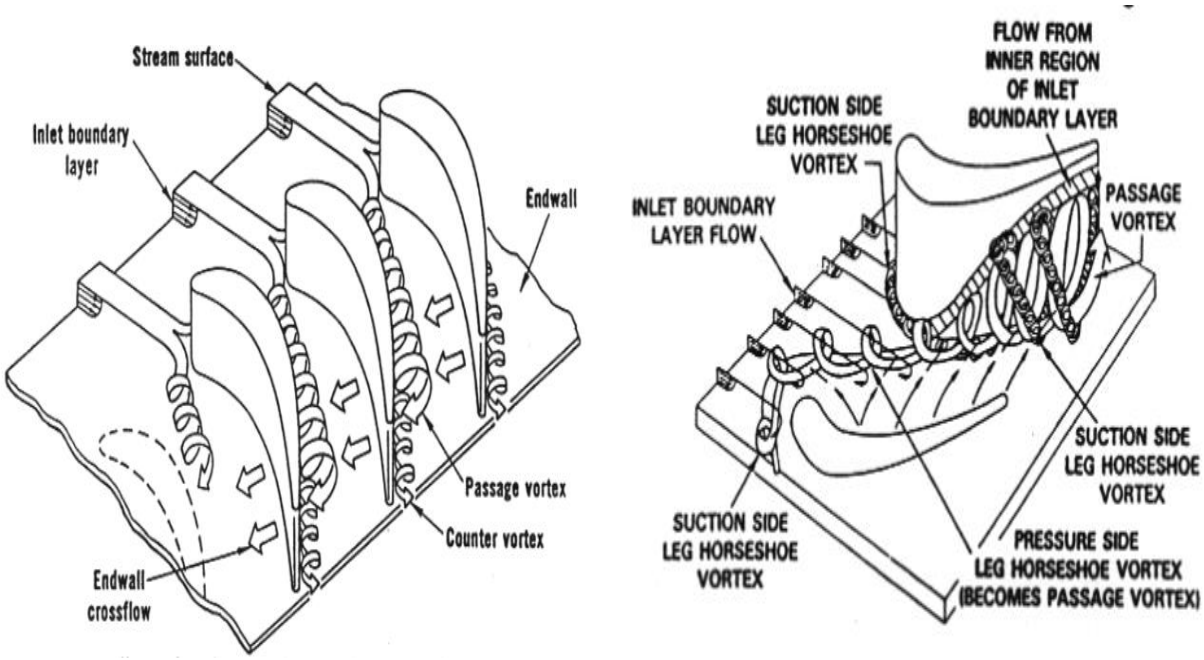


Figure 1-3 End wall Secondary Flows Visualization [3] [4]

### 1.1.2 Passage Vortex

The Passage Vortex (PV) is generated due to the same boundary layer interactions and crossflow in the turbine passage. The Euler equation for inviscid flows is useful in understanding the generation of secondary flows/vortex structures. This passage vortex can be understood using the radial equilibrium equation indicated in Equation 1-1. This equation represents the balancing of pressure forces with the centrifugal forces of a fluid particle. Due to the curved nature of steady streamline, centrifugal pressure gradient forces will be acting on the streamline fluid particles.

$$\frac{\partial p}{\partial n} = \rho \frac{v^2}{R}$$

.....Equation 1-1

From Figure 1-4 below, it can be seen that, due to the concave nature of the blade, there exists a higher pressure on the pressure side of the blade and lower pressure on the suction side of the blade. This pressure difference forces the flow to turn. Further, due to the presence of the boundary layer near the hub and casing surface, the tangential flow velocity is reduced. With a constant pressure gradient, based on Equation 1-1, it can be understood that as velocity decreases, the radius of curvature (R) must decrease as well. Thus, the slow-moving fluid near the wall is compensated by the crossflow generated due to the turning of the blades. Overall, it leads to three-dimensional passage vortex generation which results in momentum deficit regions in the turbine passage.

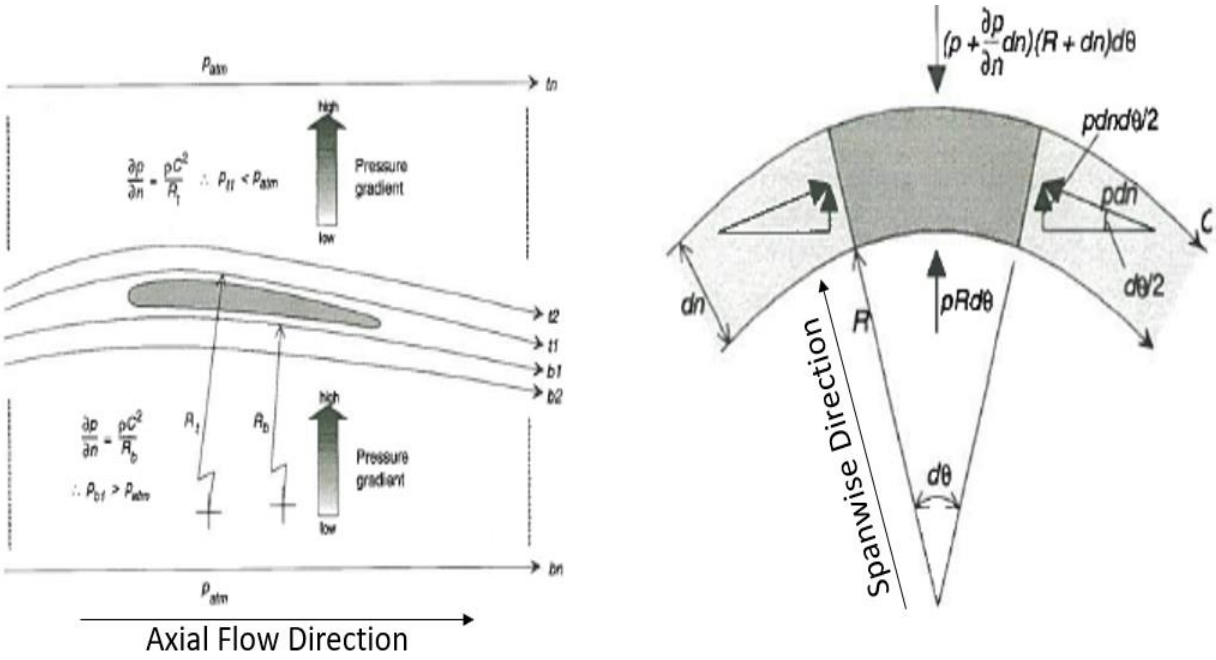


Figure 1-4 Physical Representation of n-Euler Equation [5]

Sieverding's [6] smoke wire visualization techniques were instrumental in observing the secondary flow structures near the tip region. In his experimental work on linear turbine cascade, a sun and planet analogy was used to explain the PS-HV, SS-HV and TPV, as shown in Figure 1-5. As flow approaches the blade leading edge, two counter-rotating vortices start to roll up. The left side vortex, denoted with $H_p$, is the pressure side leg of the HV (PS-HV) and right-side vortex, $H_s$, is the suction side leg of the HV (SS-HV). As the flow moves downstream, PS-HV moves upwards and SS-HV is shifted slightly downwards. Behind the blade passages, PS-HV and SS-HV are merged which is difficult to differentiate. Hence, it is called as Tip side Horseshoe Vortex (THV) in further sections as it is generated near the casing endwall. Also, due to crossflow, passage vortex is formed near the tip section. This tip passage vortex (TPV) is the counterpart of the passage vortex generated near the hub (HPV). The TPV rotates in the same sense of rotation as PS-HV.

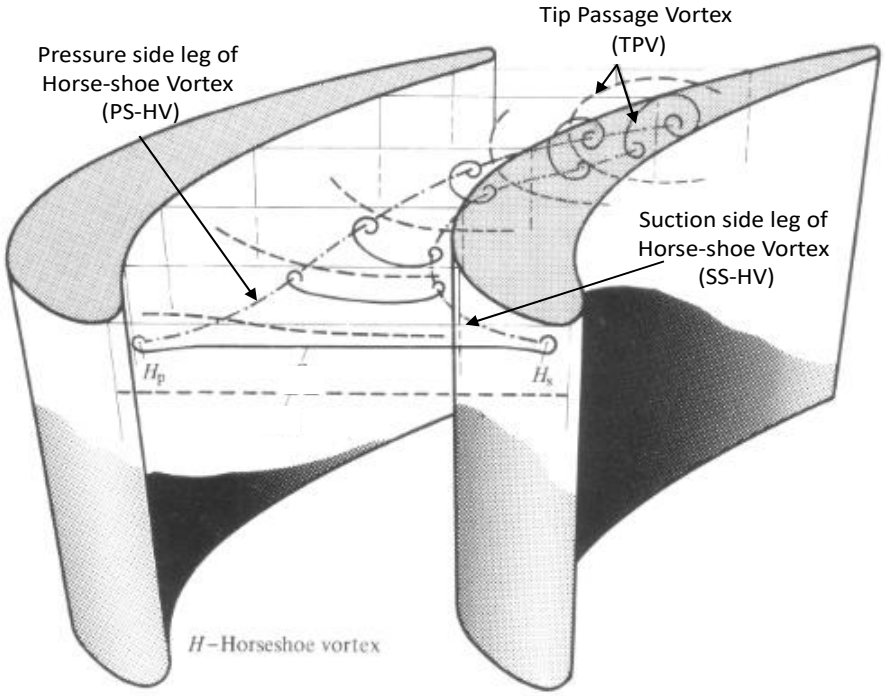


Figure 1-5 Evolution of Horseshoe and Passage Vortices through a Linear Turbine Cascade [6]

### 1.1.3 Tip Leakage Vortex

A small gap is present in between the blade tip and casing to avoid the mechanical rubbing of the rotating blade against the stationary casing. This gap cannot efficiently extract the energy from the hot fluid as it is passed to the other side of the blade without turning. This leakage flow leads to tip leakage losses which account for approximately 30% of the total aerodynamic losses in a turbine stage [7]. Tip leakage loss is usually considered as a parasitic loss in the turbine stage. Due to the pressure difference between the suction side and pressure side, flow exits the suction side with a higher velocity at an oblique angle relative to the passage flow. This strong leakage flow interacts with the incoming passage flow causing the Leakage Vortex (LV) to roll up into a streamwise vortical structure. Figure 1-6 illustrates the cross-section of the rotor blade, on top of which flow is

moving from the Pressure Side (PS) to the Suction Side (SS) through the tip gap. As the flow passes, there is a bubble generated denoted as b1, due to separation. Apart from parasitic losses generated by the tip leakage losses, the momentum deficit generated due to tip-leakage vortex is also propagated further to the next stages. This momentum deficit adversely affects the subsequent stages and reduces their aero-thermal efficiency.

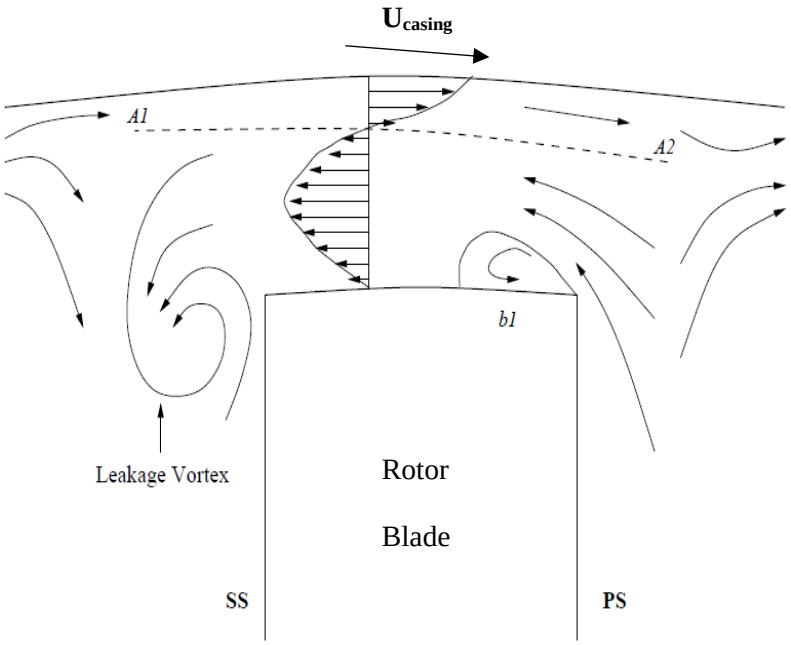


Figure 1-6 Schematic of Leakage Flow-Field near Turbine Rotor [24]

The gap between the blade and casing is very small (less than 1 mm), such that it is very difficult to reduce the gap any further. Apart from tip clearance studies, many tip desensitization studies have been conducted to reduce the tip losses. Dey and Camci [24] performed experimental studies using partial squealer ribs. It was found that the suction side squealer reduces the total pressure deficit to a certain degree. Andichamy [8] performed turbine slit studies that could counteract the leakage vortex. In all the studies of modifying the blade tip region, an attempt was made to reduce leakage mass flow rate through the tip which would be eventually helpful in weakening the tip-leakage losses. Alternatively, the tip-leakage losses can be reduced by also modifying the casing surface. Groove patterns on the casing surface would impede the flow if oriented in a proper direction. Various casing design patterns are available for the compressor region, where the circumferential grooves are helpful to delay the stall [22] [23]. Nevertheless, for the turbine region, there are very few casing related research studies available in the open literature. Rao [10] conducted experiments by increasing the surface roughness of the casing. Gumusel [9] found during experimentation, that the curved patterns on the casing could reduce the aerodynamic losses associated with the tip. Kavurmacioglu [11] observed improved aerodynamic performance for the circumferential groove design for a stationary linear cascade model. The current study is performed in a rotational frame of reference with a computational model similar to the experimental setup present at Axial Flow Turbine Research Facility (AFTRF). The aim is to generate a comprehensive fluid dynamic understanding of the casing groove patterns in HP turbine stages. Experimental measurements from a single-stage, large scale rotating turbine facility and 3D RANS computations are utilized to investigate the main flow features and performance attributes of the casing patterns under investigation.

### 1.2 Axial Flow Turbine Research Facility (AFTRF)

Axial Flow Turbine Research Facility is a test facility in the Department of Aerospace Engineering at Pennsylvania State University. AFTRF is a High pressure (HP), open loop, low speed, single-stage, and cold flow axial-turbine facility, which was built mainly to study the steady/unsteady/turbulent three-dimensional passage flows. The schematic of the AFTRF facility is as shown in Figure 1-7. A detailed description of the facility is presented in the Lakshminarayana [12] and Camci [13]. There are 26 NGV and 29 rotor blades in the setup. The rotor speed can be adjusted between 175 and 2000 RPM. For this research, the rotor was kept at 1330 RPM within +/- 1 RPM. The design parameters of the facility are tabulated in Table 1-1.

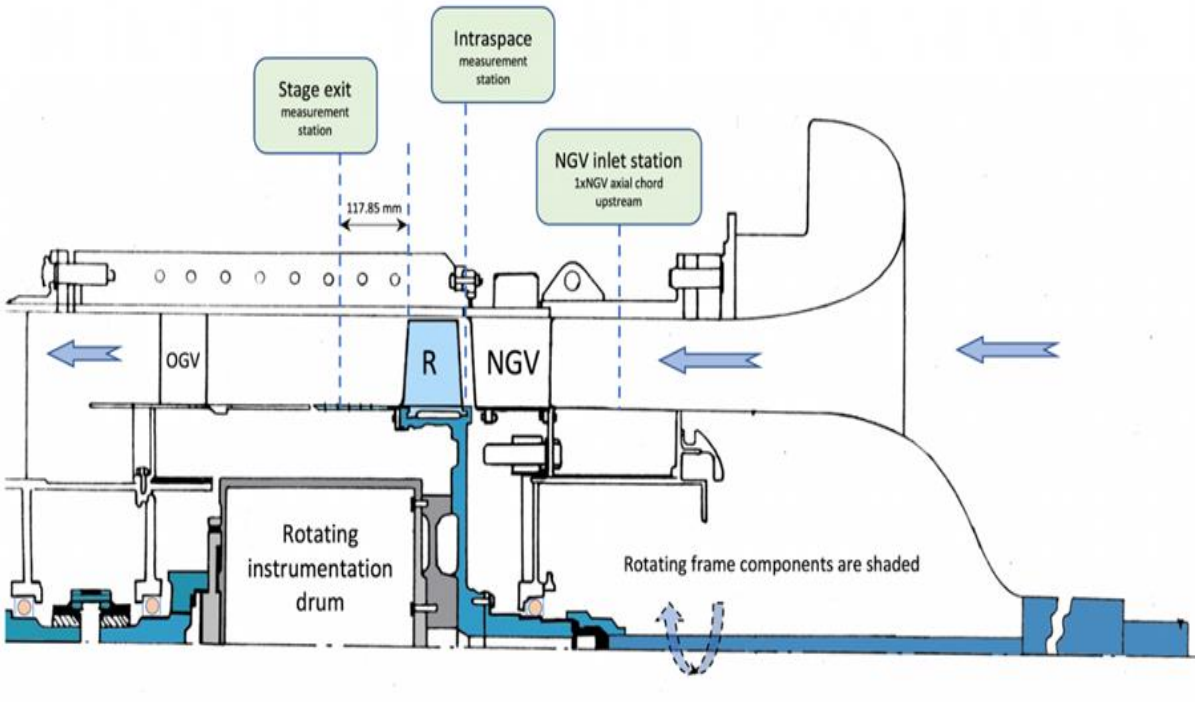


Figure 1-7 AFTRF Test Facility [15]

Table 1-1 AFTRF Design Parameters

| | |
|---|---|
| Total temperature at the inlet (K) | 289 |
| Total pressure at the inlet (kPa) | 101.360 |
| Mass flow rate (kg/s) | 11.05 |
| Rotational speed (RPM) | 1300 |
| Total pressure ratio ($P_{01}/P_{03}$) | 1.0778 |
| Total temperature ratio ($T_{03}/T_{01}$) | 0.981 |
| Pressure drop(mmHg) ($P_{03}$-$P_{01}$) | 56.04 |
| Power (kW) | 60.6 |
| Stator efficiency | 0.9942 |
| Rotor efficiency | 0.8815 |
| Total-to-Total isentropic efficiency | 0.8930 |

The rotor blade has a small gap between its tip and casing surface, which is called the tip-clearance gap. The tip-clearance ratio (t/h) is the ratio of the tip clearance gap divided by the blade height. The tip clearance ratio for the simulations and experimental set-up was fixed at 0.8%. As the blade height is 122.9 mm, the tip clearance is approximately 1 mm. The blade and vane data of the turbine stage are presented in Table 1-2.

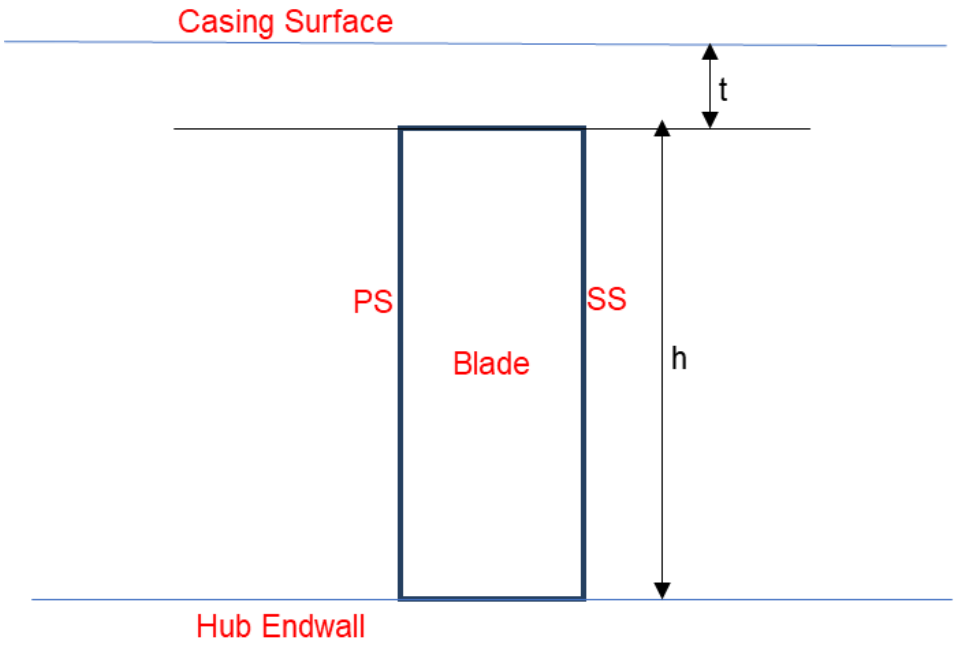


Figure 1-8 Schematic of Tip Clearance ratio

Table 1-2 AFTRF Rotor Blade Parameters

| | |
|---|---|
| Rotor hub-tip ratio | 0.7269 |
| Blade tip radius (m) | 0.4582 |
| Blade height, h (m) | 0.1229 |
| Relative Mach Number | 0.24 |
| Number of Blades | 29 |
| Axial Tip Chord (m) | 0.085 |
| Spacing (m) | 0.1028 |
| Turning angle, tip/hub (deg) | 95.42/125.69 |
| Nominal Tip Clearance (mm) | 0.98 |
| Reaction, hub/tip | 0.197/0.519 |
| Reynolds Number ($-10^5$) inlet/exit | (2.5-4.5)/ (5-7) |
| Tip Clearance Ratio (t/h) | 0.8% |

### 1.3 Objectives and the Structure of the Thesis

The primary objective of this study is to perform computational analysis of different casing patterns placed on the inner side of the outer endwall. The secondary objective is to validate the computational data against the experimental data collected. The aerodynamic experiments for the turbine stage were conducted in AFTRF under the influence of casing patterns. Subsequent to validation, further investigations examined the flow physics. The study paves way for a better understanding of different flow aspects due to casing patterns. This also helps in the performance characterization of the turbine stage. Analysis of different vortex structures like Leakage Vortex (LV) and Tip Passage Vortex (PV) generation near the blade tip plays a significant role in this study. Based on this understanding, the goal is to develop an improved design that could reduce leakage losses and enhance the performance of the system.

The thesis is organized into six chapters. Chapter 2 deals with the modeling of the turbine stage. It explains the CAD model developed in house and the boundary conditions utilized for the computational set-up. The flow physics modeling used for the simulations is also explained. It also explains the rationale for selection of a specific turbulence model which was utilized for the computational simulations. Finally, it provides details of the grid dependency study and validation of the optimized baseline grid results with the experimental results.

Chapter 3 discusses the geometry of three preliminary casing designs. It describes the validation study performed for the NGV and rotor section. The pressure coefficient results at mid-span of NGV and rotor blade for all the casing designs are compared with corresponding data obtained from the baseline design.

Chapter 4 discusses the results of the analysis. The results from computational as well as experimental results are analyzed. Measurement plane details are described, and pressure contour plots are discussed. The pressure contour plots are useful to visualize the vortex structures. The performance parameter known as the Figure of Merit (FOM) is also explained and compared for experimental and computational studies. The latter part of chapter 4 involves a discussion about the three-dimensional flow visualization plots for all the three preliminary casing designs from computational simulations. Different contour plots and streamlines are discussed in detail to understand the positive and negative effects of each of the designs.

In chapter 5, an improved design is suggested based on the results for the preliminary casing design. Furthermore, the performance parameter, FOM, is calculated for better comparison with the other designs. The flow physics analysis of different vortex structures is discussed using the streamlines feature.

The summary and conclusion of this research work are presented in chapter 6. It also includes recommended future work based on the research findings. In the appendix section, the schematic of AFTRF is present. It also includes a discussion on efficiency for a low-speed AFTRF turbine and a high-speed realistic engine. Also, efficiency data for all the designs are discussed in comparison to the baseline design.

# Chapter 2

# Computational Modelling and Simulation Set-up

This chapter discusses the CAD model developed to replicate the aerodynamic details of the experimental turbine stage (AFTRF). Further, different aspects of turbulence models and complete simulation set-up is explained. A grid dependency study to optimize computational cost and processing time is elaborated upon. This chapter also includes an attempt to validate the computations against measured AFTRF data.

## 2.1 Computational Set-up

A 3D CAD model of a single turbine stage domain consisting of Nozzle Guide Vanes (NGV) and rotor blades was developed. The 3D CAD model of the ARTRF airfoils was modeled based on 3D scanning of the blades obtained from a precise 3D laser scanning system. The final solid model of the system is a high-resolution and high accuracy model. The entire turbine stage with casing hidden is shown in Figure 2-1.

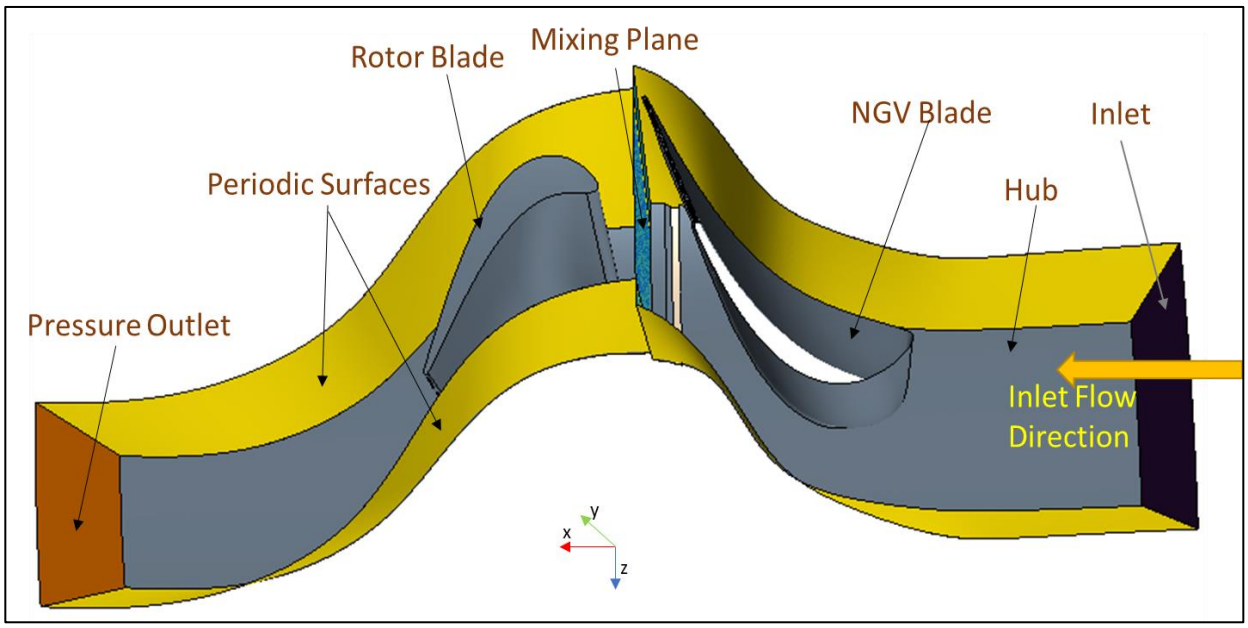


Figure 2-1 Single Blade Fluid Domain consisting of NGV Section (left) and Rotor Section (right)

Star-CCM+ [14], a general-purpose computational fluid dynamics solver, was used for the geometry processing, meshing, multiphysics simulations, post-processing and other aspects of simulation workflow. It has in-built different turbulent solvers. It can automate the entire process from geometry processing to post-processing which helps to optimize time while analyzing different designs. A single blade control volume was used for analysis in Star CCM+ using periodic boundary conditions on the pressure and suction sides of the blades. Although the periodic surfaces are separated in space, they can be mapped to each other using a constant rotational factor. Thus, the two periodic surfaces act like a symmetric plane. The periodic boundaries are located approximately between the fluid domain of the two blades. A periodic boundary condition feature is used to model one blade passage. It is instrumental in saving the processing time and size of simulation. It is possible to simulate the periodic results for all the blades and stages after the post-processing. Most of the solid surfaces were termed as wall boundaries. It includes NGV blade surface, casing, endwall and rotating rotor blades. A no-slip condition is used near the wall boundaries. The boundary conditions and physics of the simulations were taken as a reference from past computational studies by Doshi [15].

**NGV stage:** Inlet is located one chord upstream of the NGV blade. The boundary condition for the inlet region was specified as a “velocity inlet”. The velocity profile at the inlet section in the spanwise direction can be seen in Figure 2-2. This velocity profile is based on the experimental data obtained by Zaccaria [16]. The turbulence intensity and total pressure at the radial locations, shown in Figure 2-3, were provided at the inlet based on a reference pressure of 100839 Pa. The turbulent length scale was specified as 7.5 mm. NGV is stationary and there is no gap in between the blade tip and casing of NGV. The NGV stage involves a purge section on the hub side near the outlet. Purge is a leaking outlet from the rim-seal cavity with 0.0046 kg/s mass flow rate, as studied

by Averbach [17] in an experimental study. The NGV outlet is an interface to the rotor inlet, located at 1.025 chords downstream of NGV blade's midspan trailing edge.

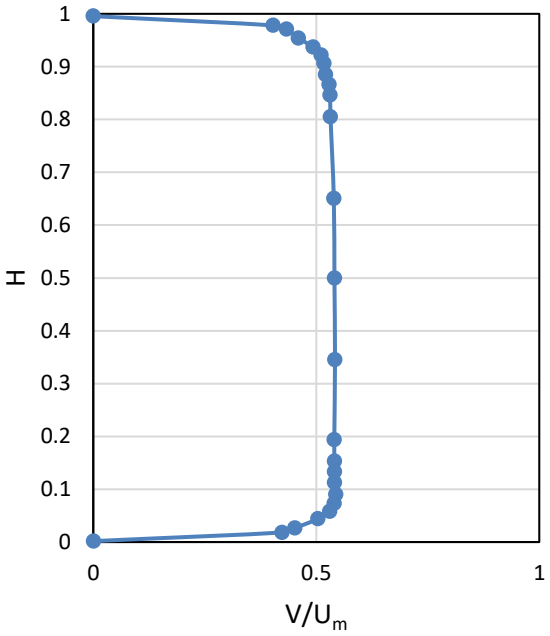


Figure 2-2 Inlet Boundary Conditions: Spanwise Distribution of Velocity

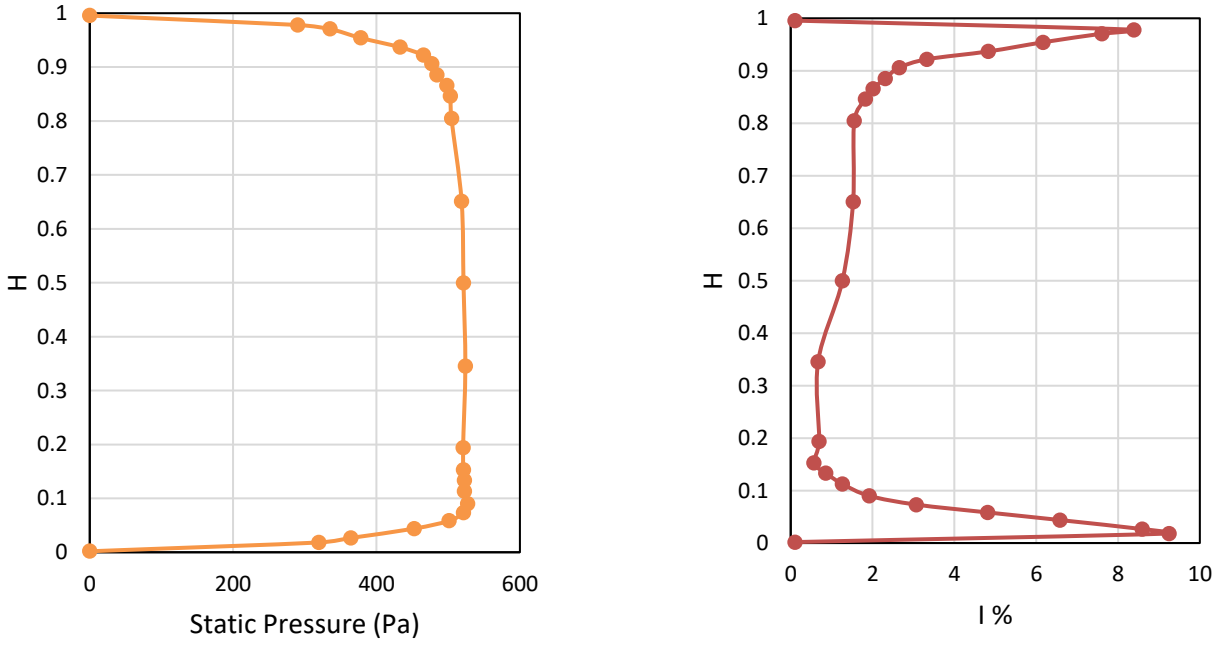


Figure 2-3 Inlet Boundary Conditions in Spanwise Distribution:

Static Pressure (left) and Turbulence Intensity (Right)

**Rotor Stage:** In the rotor stage, blades are rotating at 1300 RPM. To avoid interference with flow inside the computational domain, the rotor outlet is 1.5 chords downstream of the rotor blade trailing edge from the blade tip surface. The radial equilibrium condition is specified near the outlet to govern the mass flow rate according to the experimentation stage. The target mass flow rate was set to be 10.63 kg/s with pressure outlet conditions. The turbulence specifications were "turbulent kinetic energy", $k$, and "specific dissipation rate", $\omega$. The "specific dissipation rate", $\omega$ was specified as 2000/s and turbulent kinetic energy values were calculated and provided at the rotor outlet for every next iteration to achieve a quick convergence rate. The rotor inlet is close to the rotor blade to have an inlet perpendicular to flow direction and to accommodate the purge section properly. All results presented for this study are based on steady flow simulations. The flow from the stationary NGV stage is passed into the rotating rotor stage using Mixing Plane i.e., a stationary to rotating interface.

**Mixing Plane Interfaces:** Interfaces are used to transfer solution quantities between different regions in the simulation. Periodic surface interfaces are used in the simulation to reduce the size of the simulation domain. The mixing plane is an essential interface in multi-stage turbomachinery flows. The NGV is stationary and the rotor blade is rotating with stationary casing. In order to transfer the solution quantities such as mass, momentum, energy terms from NGV to the rotor stage there arises the requirement to have a mixing plane interface. It is helpful to transfer all the quantities using the circumferential averaging technique. Thus, the final solution of the flow quantities is in radially varying direction. The NGV outlet serves as the mixing flow outflow boundary from where the flow quantities are circumferentially averaged. Inputs are provided at the rotor inlet section and hence, rotor inlet acts as mixing flow inflow boundary. As an implicit approach is used to get a solution across the mixing plane, it gives one additional degree of freedom per variable per circumferential bin.

## 2.2 Flow Physics Modeling

The three-dimensional model along with turbulent flow was used for all computational simulations. The experimental set-up is a low-speed turbine facility with relative Mach Number less than 0.3. It is useful to simplify the set of equations by using Ideal Gas relations in the CFD model as the compressibility effects are not very strong. The flow equations are solved in an uncoupled manner. Star-CCM+ provides two options to solve the flow equations: one is a coupled model and the other one is a segregated (uncoupled) flow model. Coupled flow is usually used for models with compressible flows at high Mach Number. The segregated flow model is usually a suitable method for compressible flows with low Mach Numbers. Therefore, for this study, a segregated flow model was utilized to solve flow equations i.e. one for each component of velocity in momentum equations and one for pressure in the continuity equation. Initially, the momentum equations were solved to get velocity components. Subsequently, the pressure-correction equation was solved to update the pressure, mass flow rate, etc. Predictor correct approach based on the SIMPLE algorithm was used for the linkage between the two equations. The rest of the equations were solved in a stepwise manner. Each variable is solved for all the cells and convergence is checked. For the energy equation, thermal enthalpy was selected as a variable by using the Segregated Fluid Enthalpy model. It makes use of enthalpy to compute the temperature from the equation of state.

To solve any fluid and thermodynamic related problem, it is required to solve the range of Navier-Stokes Equations. However, computational simulations have their own limitations to solve them entirely. Usually, averaging is carried out by some approximations and mathematical treatments which resulted in popular Reynolds-Averaged-Navier-Stokes (RANS) equations. Thus, steady numerical simulations are performed by solving three-dimensional RANS flow equations using finite volume formulation. Apart from basic mass, momentum and energy equations, it makes use

of some auxiliary equations like Equations of State, Stokes hypothesis and Sutherland's law. In recent times, RANS equations have proved to be the most suitable equations to study simulations involving three dimensional, viscous and turbulent flows in the rotational frame of reference. Large Eddy Simulations (LES) and Direct Numerical Simulation (DNS) are also very useful for flow physics study but they are time-consuming as well as expensive methods.

To accurately predict the flow leaking through the tip gap, the SST $k-\omega$ turbulence model with gamma-transition is employed. $k-\omega$ is the two-equation model useful to solve transport equations for the turbulent kinetic energy, $k$, and specific dissipation rate, $\omega$. The turbulence models are useful to determine the turbulent eddy viscosity. The Reynolds stress tensor in momentum equations adds six more additional unknowns in the momentum equation. The $k-\varepsilon$ model was studied for the simulations, but it has some limitations which were visible in the post-processing. Based on the results and the equations utilized, it could not properly model adverse pressure gradients, strong curvature flow regime and no-slip walls. This is because there is always a difficulty in solving for the $\varepsilon$. The $k-\omega$ model also has its own limitations, as the boundary layer computations are sensitive to $\omega$ in the free stream. However, the SST $k-\omega$ model is blend of $k-\varepsilon$ and $k-\omega$ models which was proposed by Menter [18]. In general, this model utilizes $k-\omega$ turbulence model near the walls to solve for boundary layer effects whereas $k-\varepsilon$ is utilized away from the walls to capture large eddies. Thus, the transformed equation adds an additional non conservative cross-diffusion term.

The turbulent kinetic energy k as derived by Menter is,

$$\frac{\partial(\rho k)}{\partial t}+\frac{\partial\left(\rho u_j k\right)}{\partial x_j}=P-\beta^{*}\rho\omega k+\frac{\partial}{\partial x_j}\left[(\mu+\sigma_k\mu_t)\frac{\partial k}{\partial x_j}\right]$$

.....Equation 2- 1

The dissipation rate $\omega$ can be solved using the below equation,

$$\frac{\partial(\rho\omega)}{\partial t}+\frac{\partial\left(\rho u_j\omega\right)}{\partial x_j}=\frac{\gamma}{\nu_t}P-\beta\rho\omega^2+\frac{\partial}{\partial x_j}\left[(\mu+\sigma_\omega\mu_t)\frac{\partial\omega}{\partial x_j}\right]+2(1-F_1)\frac{\rho\sigma_{\omega2}}{\omega}\frac{\partial k}{\partial x_j}\frac{\partial\omega}{\partial x_j}$$

.....Equation 2- 2

### 2.3 Grid Dependency Study

Meshing in CFD is most important to resolve the vortical flow structures, and the final grid quality has a severe impact on the accuracy of the CFD solution. There are different methods available for meshing, such as unstructured grid and structured grid, which also includes the C, H or I type grids. For the steady numerical simulations, an unstructured grid was suitable to develop using the Star-CCM+ mesh solver. Different input control parameters governed the grid development. The model was discretized using polyhedral cells in an unstructured grid. The entire volumetric mesh with cell distributions can be seen in Figure 2-4.

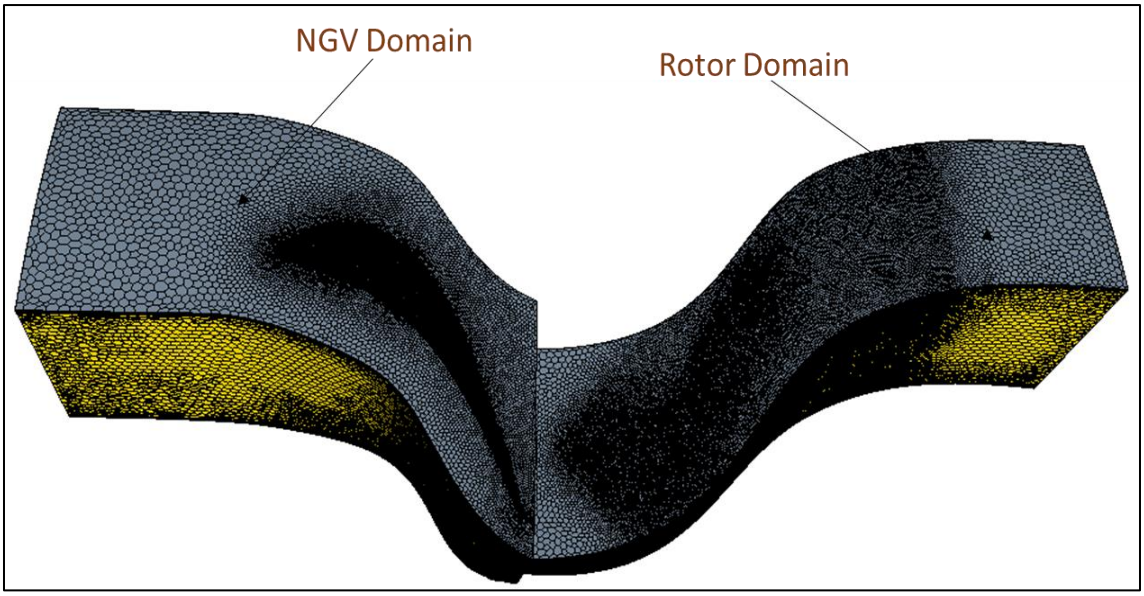


Figure 2-4 The Volumetric Mesh of NGV Section (left) and Rotor Section (right), 3-D view from the Casing Side.

In order to study the flow physics near the tip and casing surface, a finer mesh with prism layers were employed in the tip gap. Prism layers were also used near blade surfaces, as shown in Figure 2-5, to capture boundary layer interactions. The finer mesh was made in the blade wake region to capture secondary flows near the measurement plane used in experimentation.

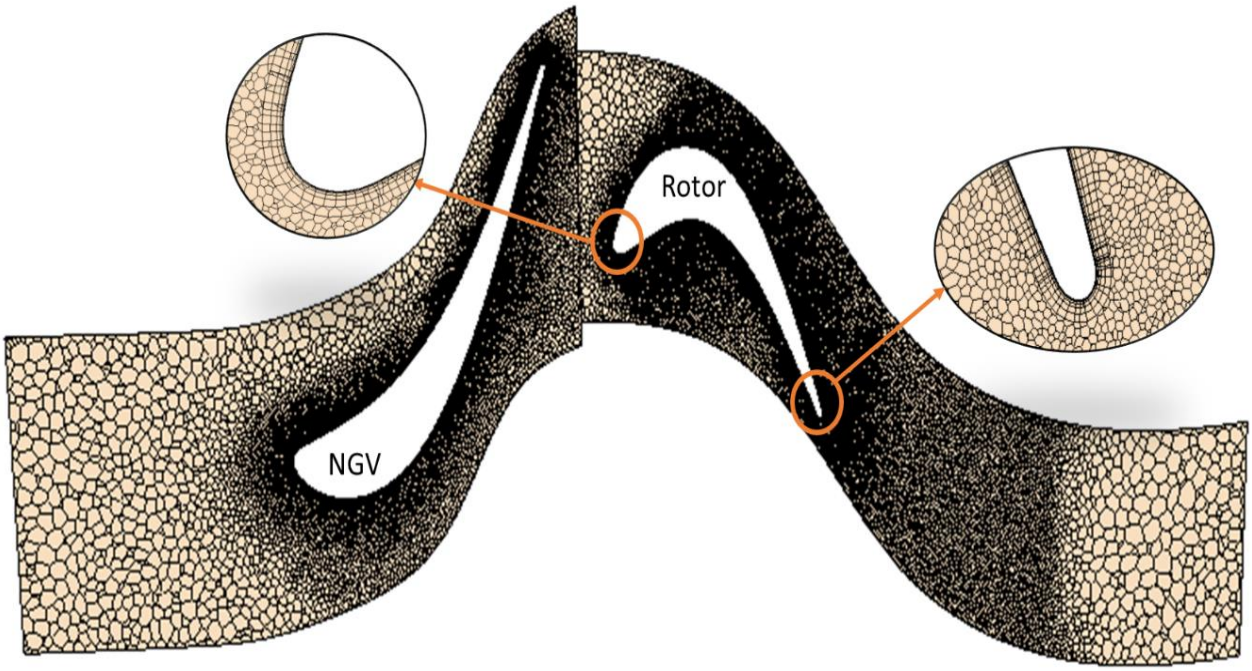


Figure 2-5 Blade Mid-Span Cross-Section with Prism Layers Detailed near the Blade Edges

Three different meshes were studied in order to find a suitable mesh that provides accurate results in a lower computational time. The mesh studies were performed for NGV as well as the rotor section. The details of the three mesh studies done for the NGV section are available in Table 2-1. The wall y+ value for each of the mesh studied was below 1. While performing this study, cells in the rotor section were kept constant as 5.3 Million.

Table 2-1 Mesh Details for NGV Mesh Study

| **Mesh Type** | **Cells in NGV domain (million)** | **Cells in Rotor domain (million)** |
|---|---|---|
| Fine Mesh | 5.2 | 5.3 |
| Optimized Mesh | 4.3 | 5.3 |
| Coarse Mesh | 3.1 | 5.3 |

Static pressure values (p) at the mid-span of the NGV blade were obtained from the simulations of the three meshes. Using these pressure values, the static pressure coefficient ($C_p$) was calculated for the studies using equation 2-3. The calculated $C_p$ can also be called as blade loading coefficient. NGV blade loading data from the AFTRF experiments were obtained from Zaccaria [16] as shown in Figure 2-6. The static-pressure coefficient data for the three different meshes are also plotted with respect to the non-dimensional axial location of the blade. The comparison shows that optimized and fine mesh, both show less deviation from the experimental results. However, the coarser mesh had a higher deviation from the experimental data. Hence the optimized mesh with 4.3 Million cells in the NGV domain was selected to optimize the computational resources.

$$Static\ Pressure\ Coefficient, C_p = \frac{p - P_{o1,avg}}{0.5 * \rho * W_{x1,avg}^2}$$

$$\ldots\ldots\ldots\ldots\ldots\ldots\ldots\ldots \text{Equation } 2-3$$

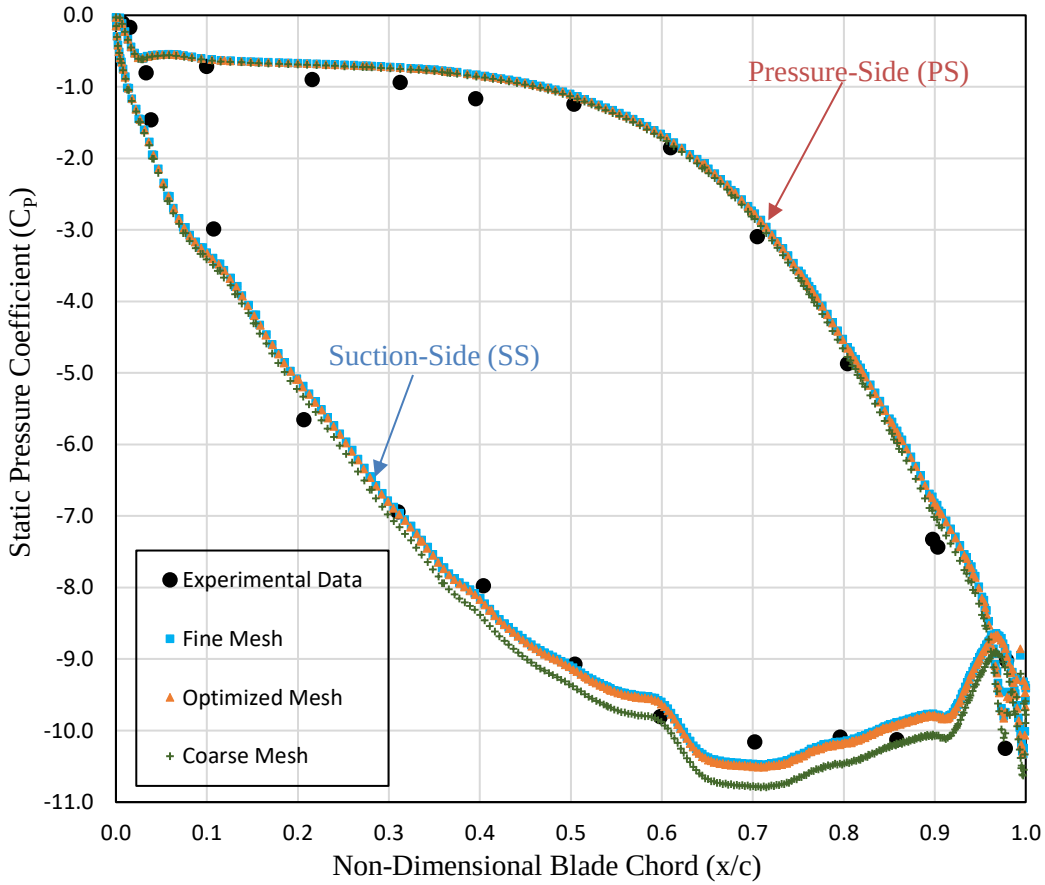


Figure 2-6 Pressure Coefficient at Mid-span of NGV Blade

Once the mesh in the NGV section was finalized, the mesh study was performed for the rotor section in a similar manner. With the NGV having a fixed number of cells, the rotor domain had three different meshes called “Fine”, “Optimized” and “Coarse” mesh with 7 Million, 5.3 Million and 3.9 Million cells respectively. These details are presented in Table 2-2.

Table 2-2 Mesh Details for Rotor Mesh Study

| **Mesh Study** | **Cells in NGV domain (million)** | **Cells in Rotor domain (million)** |
|---|---|---|
| Fine Mesh | 4.3 | 7 |
| Optimized Mesh | 4.3 | 5.3 |
| Coarse Mesh | 4.3 | 3.9 |

For the rotor mesh study, the static pressure coefficient ($C_p$') was utilized to compare the different mesh structures. The computed ($C_p$') is also compared to the AFTRF measurements. The experimental data for the $C_p$' were obtained from the Chernobrovkin [25] who completed research on the same AFTRF configuration with identical boundary conditions. The static pressure coefficient at the mid-span of the rotor domain (H = 0.5) was calculated using Equation 2-7. The experimental results were compared with the simulation results for all three mesh, shown in Figure 2-7. There is a good agreement of simulation results with the experimental set-up. The coarse mesh has some deviation near the mid-axial locations and the fine mesh has higher values along the pressure side of the blade near its trailing edge. Therefore, optimized mesh with 5.3 Million rotor cells was finalized for future simulation studies.

$$Static\ pressure\ Coefficient, C_p' = \frac{p - p_{3_{avg}}}{0.5 * \rho * W_{x2,avg}^2}$$

.....Equation 2- 4

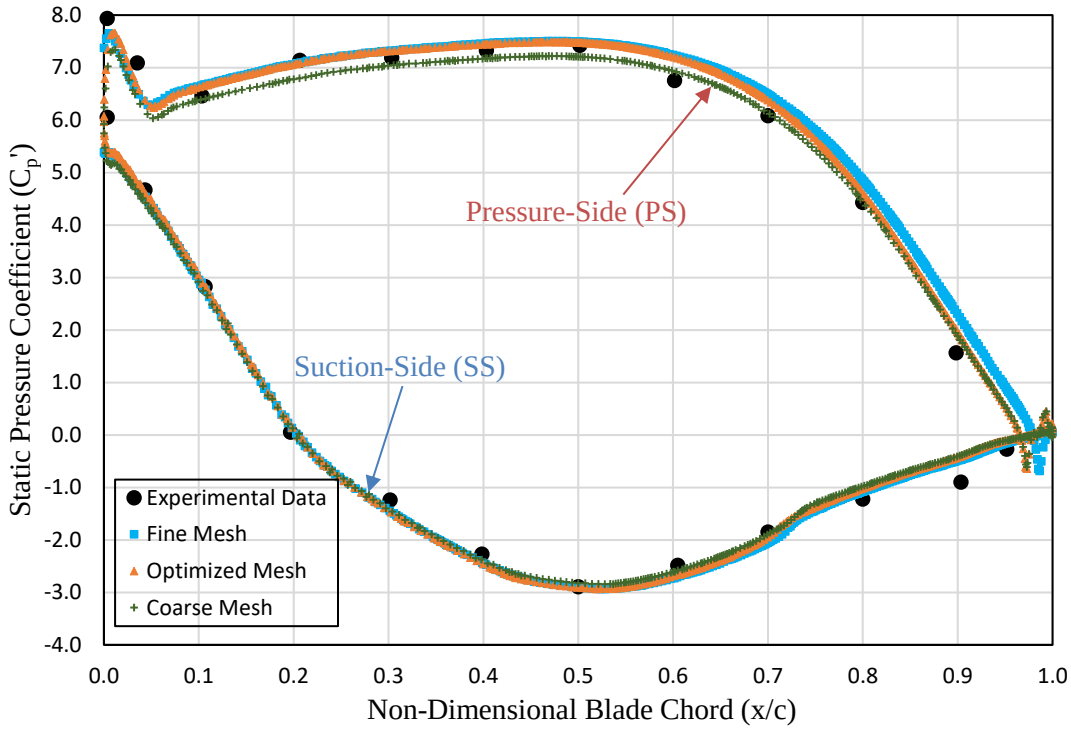


Figure 2-7 Static Pressure Coefficient at Midspan of Rotor Blade

All simulations were performed in-house using the parallel computing Cocoa 4 cluster (cocoa4.aero.psu.edu) present at Pennsylvania State University in the Department of Aerospace Engineering. Cocoa4 comprises of 54 computational nodes. Each computational node is made up of two quad-core Intel® Xeon® Processor E5430. The processor has a base frequency of 2.66 GHz. Each node in the cluster has eight cores and 8 GB of RAM. The cluster has a disk storage space of 2TB. It also has a computational network fabric with InfiniBand of 20 Gb/s. There were 21 nodes utilized each having a processing speed of 2.66 GHz. 2700 iterations were required for all the simulations to obtain converged solutions. In general, residuals for continuity, momentum and energy equations were converged to a level of $10^{-4}$. The turbulent kinetic energy and other parameters had residuals below a level of $10^{-5}$. Thus, for complex turbomachinery applications, a good level of convergence criteria was achieved for all transport equations used.

# Chapter 3

# Casing Designs Modifications and Validation Study

In this chapter, different casing designs are analyzed for aero-thermal improvements from unique casing patterns in an HP turbine stage. Also, a comparison of the blade mid-span pressure coefficient is discussed to understand the influence of the new casing designs on the mainstream flow near the blade mid-span.

## 3.1 Different Casing Patterns

In the initial stage of this research, different preliminary casing designs were analyzed. Simple modifications were made on the rotor casing to understand its effects on flow vortex structures and leakage losses. For preliminary understanding, three different casing patterns, “Spherical Patterns”, “Axial Grooves” and “Circumferential Grooves” were designed and analyzed in comparison to the “Baseline Design”. Figure 3-1 depicts the geometry for the casing pattern designs developed in a solid modeling tool, "SolidWorks". All the new designs were compared to the baseline design in terms of performance parameters.

Baseline design involves a smooth casing surface as seen in the top left side of Figure 3-1. The baseline term in this research study denotes a smooth casing (inner) surface that does not have any modifications. However, the rest of the designs have different profile shapes termed as patterns or grooves on the inner casing surface. In each pattern of this study, different cavity shapes are engraved on the casing surface. The changes in the geometry were only made on the rotor domain’s casing surface close to the rotor blade and there were no modifications made on the rest of the AFTRF turbine casing. Thus, the NGV stage of AFTRF facility is similar for all the current casing pattern development studies, and the rotor stage has new patterns/designs on the casing surface.

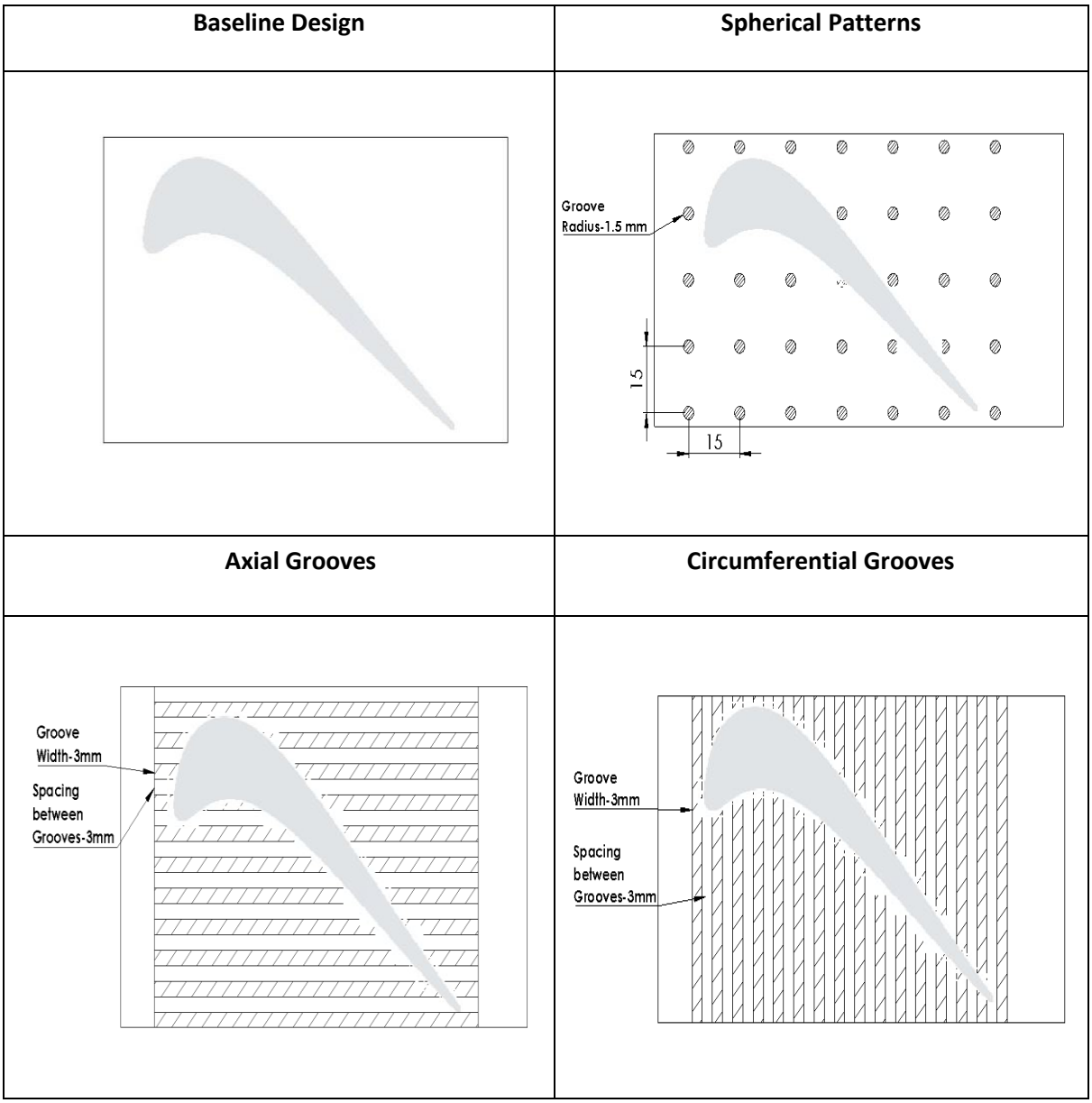


Figure 3-1 Geometry of Turbine Casing Designs

The first new casing design present on the top right side of Figure 3-1 is called the “Spherical Patterns” design. The hemisphere shaped cavities in the casing are like dimples on a golf ball. The radius of each hemisphere is 1.5 mm and it has a perfectly smooth surface. Thus, the maximum depth of the sphere is 1.5 mm at the center. The center to center distance between the two patterns is 15 mm which is kept constant in the horizontal as well as vertical direction.

The second design is called “Axial Grooves” design which can be visualized on the bottom left of Figure 3-1. As the name suggests, it has grooves present in the axial direction, running parallel to the inlet flow direction of the turbine stage. The width of the grooves is 3mm and spacing between all the grooves is kept constant at 3mm. The axial grooves also have a depth of 1.5 mm, like other designs. During the design stage of the axial grooves on the annular shape of the casing, the periodicity of a single blade control volume was taken into consideration. Due to curved periodic surfaces on each side of a rotor domain, the grooves are cut accordingly, and its continuation is present in another domain.

The third casing design, known as “Circumferential Grooves” design is shown in the bottom right of Figure 3-1. This design has grooves oriented perpendicular to the inlet flow direction. The design of circumferential grooves was not influenced by periodicity as grooves count are increasing parallel to the flow direction and not in pitch-wise direction. For a better comparison with the axial grooves design, the pertinent dimensions were kept similar. Thus, the design has groove width as 3 mm, with spacing between grooves as 3 mm and groove depth as 1.5 mm.

The above three design modifications are basic profile designs to study the effect of modifications on the flow characteristics of the turbine near the blade tip, which will eventually help to produce an improved design.

## 3.2 Validation Study for the Casing

All casing design studies have the same boundary conditions as discussed in chapter 2. The meshing structures were also similar with the same input parameters. However, as there were few additional surfaces due to the casing designs, the number of cells in the rotor section was increased slightly. The number of cells present in the NGV and rotor section for all the designs is given in Table 3-1.

Table 3-1 Grid Details for all the Turbine Casing Designs

| **Designs** | **Cells in NGV domain (million)** | **Cells in Rotor domain (million)** |
|---|---|---|
| Baseline | 4.3 | 5.3 |
| Spherical Patterns | 4.3 | 5.4 |
| Axial Grooves | 4.3 | 5.7 |
| Circumferential Grooves | 4.3 | 5.7 |

The NGV stage is unchanged for all the studies. Thus, the numerical parameters extracted from the NGV stage from all simulation studies are similar. In order to validate it for all the designs, computed total pressure coefficient values were compared as seen in Figure 3-2. The total pressure coefficient was calculated based on the Equation 2-3 at the mid-span of the NGV blade (x/h = 0.5). As discussed in the last chapter, the baseline results are in good agreement with experimental data along the pressure side as well as the suction side of the blade. Thus, it can be seen from Figure 3-2, that there is no difference in the NGV blade loading as the pressure coefficient values overlap with the baseline design. This result is helpful for the future in case there is a need to isolate the rotor section with input parameters from the NGV outlet.

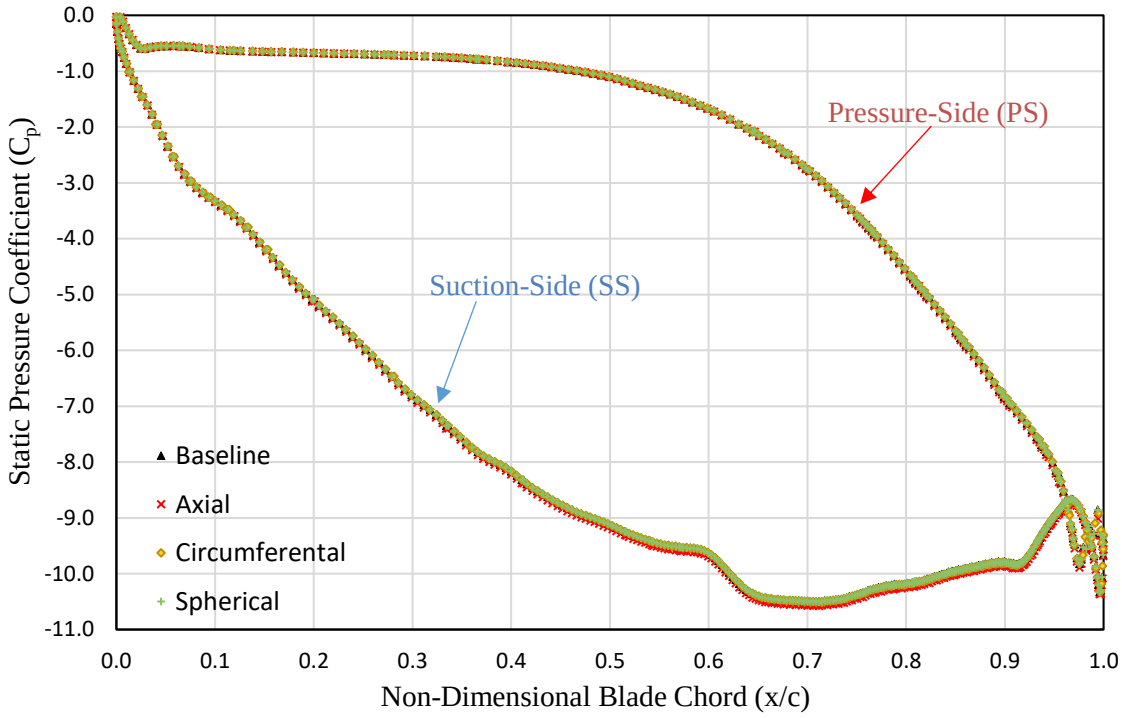


Figure 3-2 Pressure Coefficient at Mid-Span of NGV Blade

For the rotor section, computed static pressure coefficient for baseline casing design matches with the experimental data. However, with changes in grooves patterns near the rotor casing, different designs produce visible changes. The static pressure coefficient plot shown in Figure 3-3, has minor variations. This is evident for the axial grooves design which has a higher static pressure coefficient on the suction side and less on the pressure side in the mid-chord section compared to the other designs. However, the changes for all the designs are not significant for the 50% blade span because the design modifications are made on the casing surface. The maximum variation can be observed above 60% of the blade span. These changes are discussed in detail using the contour plots and numerical data in the next chapter.

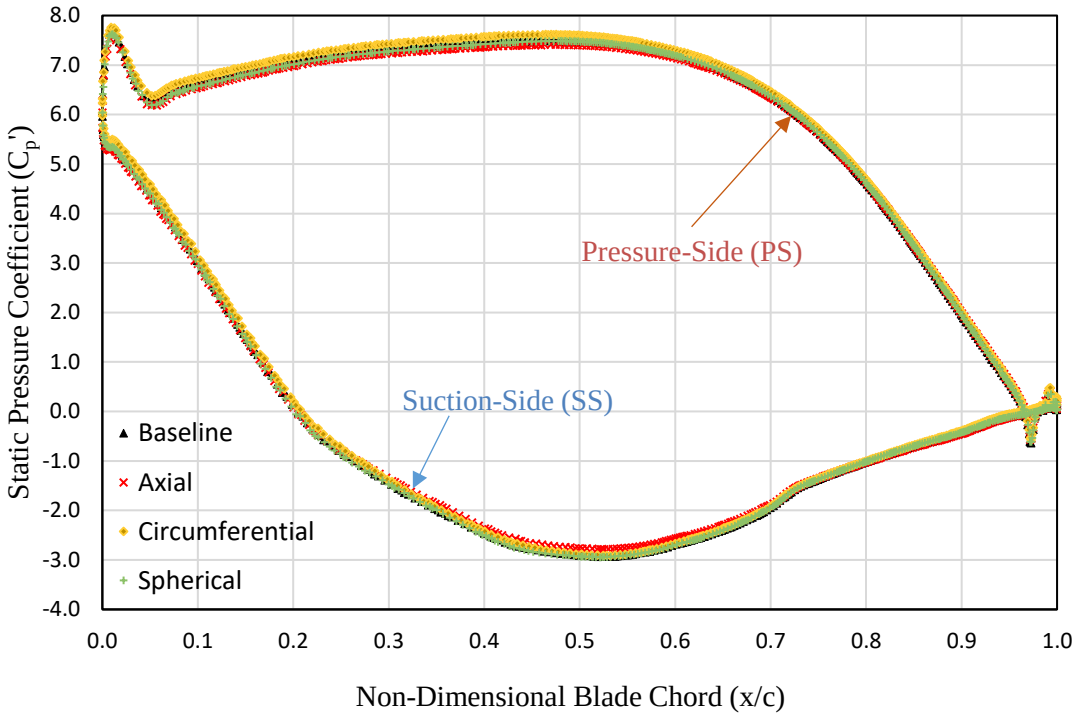


Figure 3-3 Static Pressure Coefficient Plot at Mid-Span of Rotor Blade

For all casing designs, a convergence level of $10^{-4}$ was achieved for momentum and energy terms. In addition, mass flow rate, intermittency and turbulent kinetic energy values were converged to below $10^{-5}$.

# Chapter 4

# Casing Patterns: Results and Discussions

This chapter discusses results from the computational simulations which are described in chapter 2. A steady-state solution was obtained with residuals of each parameter converging below $10^{-4}$. The results obtained from the computational study are compared to the experimental results of the three casing patterns implemented in the AFTRF. With the help of 3-D flow visualization plots and numerical data obtained from the CFD simulations, tip leakage losses for different groove patterns are analyzed further in detail. Also, the performance parameter, i.e. Figure of Merit (FOM) for each design, is analyzed in order to highlight the benefits of the new design in comparison to the baseline design. These discussions also describe the flow physics for different casing groove patterns.

## 4.1 Validation of Computational Study with Experimental Results

As discussed before, the inlet boundary conditions specified in the computational model are the same as the experimental set-up. In the experimental set-up, the Dynamic Total Pressure Probe (DTP) is located at 25.4 mm from the rotor trailing edge. The DTP probe is used to extract pressure data for million data points on a plane at that location. A detailed description of the probe and its data acquisition details are presented in Town, Akturk and Camci [20] [21]. A measurement plane at the same location is defined, and the corresponding computational results were compared to the measurements. The layout of the measuring plane can be visualized in Figure 4-1.

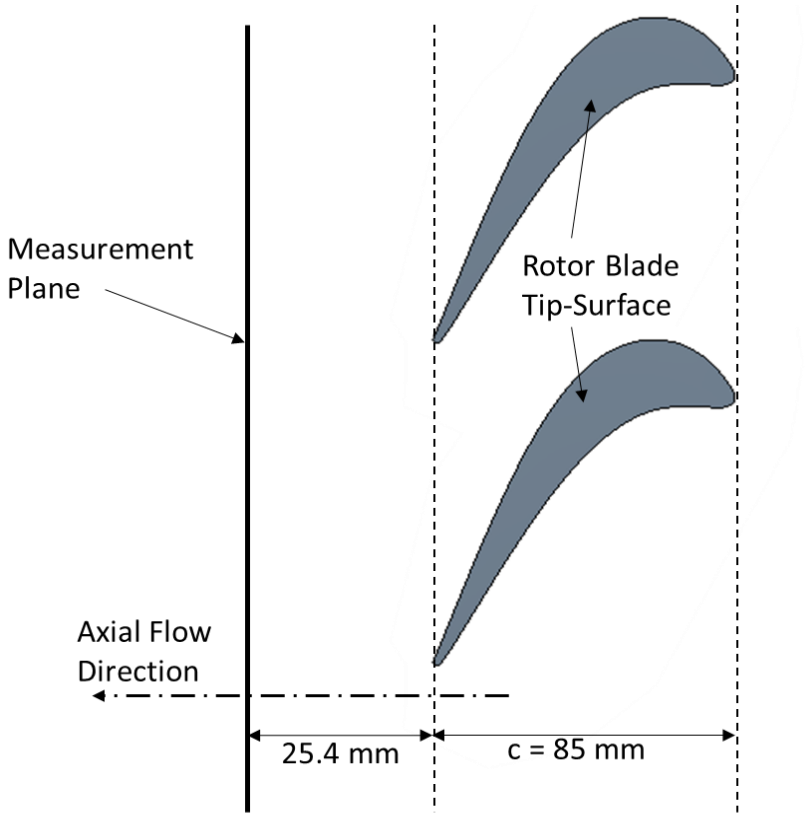


Figure 4-1 Measurement Plane of DTP Probe

The DTP probe is used to obtain the total pressure data from all 29 blade passages. The probe moves from one radial location to another linearly and was traversed from 25% to 97% span using a computer-controlled probe driving mechanism. The probe cannot cover the locations very close to the casing surface due to wall interference problems. Probe wall interference problems are visible in the last 3% span of the rotor airfoil, near the casing. The total head diameter of the probe is 5 mm. Data from the hub surface to 25% span are not captured as the focus for the investigation is to observe tip mitigation effects because of the specific casing pattern development in the turbine stage. For the experimental study, there exists blade passages with varying tip clearances. To compare with the CFD results, only data from passages # 8 and 9 were taken into consideration as they had a tip clearance of 0.8% similar to the CAD model used for simulations. The contour plots

are generated which depicts the pressure data for all designs for the two blade passages. Pressure transducer present in the DTP probe is useful to obtain the differential pressure at the measurement plane with respect to the inlet pressure data. The ensemble-averaged total pressure values are useful in determining the total pressure coefficient ($C_P$) given by Equation 4-1.

$$Total\ Pressure\ Coefficient, C_P = \frac{P_o - P_{o1_{avg}}}{0.5 * \rho * U_m^2}$$

.....Equation 4-1

The blade mean speed ($U_m = r.\ \omega$) was calculated as 54.04 m/s based on the rotor disk speed of 1300 RPM. The absolute total pressure ($P_{o1}$) at NGV inlet was measured as 101338 Pa. Due to work extraction by the turbine, pressure downstream of the rotor is less than the inlet total pressure. This results in negative values of $C_P$ at the measurement plane. Accordingly, a higher negative magnitude of $C_P$ corresponds to lower total pressure at the measurement plane. To remove the passage-to-passage data scattering and to account for the change in atmospheric conditions, a passage-averaged delta $C_P$ is calculated at each radial location. This delta $C_p$ can be calculated using passage-averaged $C_P$ and "Reference $C_P$", as shown in Equation 4-2. The "Reference $C_P$" is the arithmetic average of the $C_P$ at 10 data points in radial direction i.e., from 25% to 34% blade span. This "Reference $C_P$" is subtracted from the calculated passage-averaged $C_P$ to get the values of delta $C_P$. This value provides a better comparison as it allows for uniformity in between different experimental runs and removes passage-to-passage variations in $C_P$ values.

$$Delta\ C_P(at\ passage\ i) = C_P\ (at\ pasaage\ i) - Reference\ C_P(average\ of\ passage\ C_P\ from\ 25\%\ to\ 34\%\ BladeSpan)$$

.....Equation 4-2

Based on the equation for delta $C_P$, the contour plot of delta $C_P$ for the baseline design at the measurement plane is shown in Figure 4-2. Plots obtained from AFTRF experiment is on the left side of Figure 4-2 to validate it with the CFD contour plots shown on the right side. The contour plots for experimental and CFD studies do not have much difference in terms of flow details; the change is due to the different levels of shade in the color bars. Due to the less level of shades for experimental probe set-up, few of the low strength vortex structures are not clearly visible. This shortcoming is overcome through CFD simulations. As simulations usually provide a high-resolution image, the color bar is truncated from -0.4 to 0.4 delta $C_P$ values. The truncated color bar allows a better visualization of all the vortex flow structures. The experimental and CFD plots for the baseline design shown in Figure 4-2, exhibits similar vortex structures. An explanation about each of the vortex structures is presented as they provide a strong base for comparison with new designs at a later stage.

Different vortex structures for a smooth casing surface can be visualized in Figure 4-2. In the computational study, the vortex structures are shifted slightly towards the hub due to the presence of mixing plane between the rotor and stator. The mixing plane approach uses outlet conditions at NGV as an inlet boundary conditions for the rotor field with flow averaged in the pitchwise direction. This uniform flow can lead to movement of the vortex structures depending on the velocity directions at the mixing plane. A detailed description of the mixing plane can be found in Chapter 2.

In Figure 4-2, contour plots are represented in the spanwise direction (H). Accordingly, the endwall surface is at 0% H, and the casing surface is at 100% H. As explained earlier, experimental data is from 25% H to 97% H whereas CFD provides the data for the entire span. Arc lines in black color are marked at 25% and 97% span in the CFD plots to compare this region with the experimental

plots. To visualize the comparison in various spanwise locations, arc lines are also marked at Mid-span (50%), 80% and 90% span. These regions are useful to visualize the location of different vortex structures and core flow. The higher momentum zone shown in red color is the core area that is unobstructed by any form of boundary layer interactions. For experimental as well as computational study, it is seen that the baseline design has an almost similar profile in the center i.e. core region. Blade wake is also visible between the core areas of two blade passages. The wake, indicated in blue-green shade, extends from approximately 40% H to 80% H. Between 25% to 50% span, the effects of hub endwall boundary layer effects and secondary flow generation are visible. The low-pressure region i.e., regions in blue color represents momentum deficit regions. The momentum deficit regions are regions of high losses in the turbine flow field. Vortex present in these regions can be classified as Leakage Vortex (LV), Horseshoe Vortex (HV) and Passage Vortex (PV). The flow physics of those vortex structures are discussed in Chapter 1.

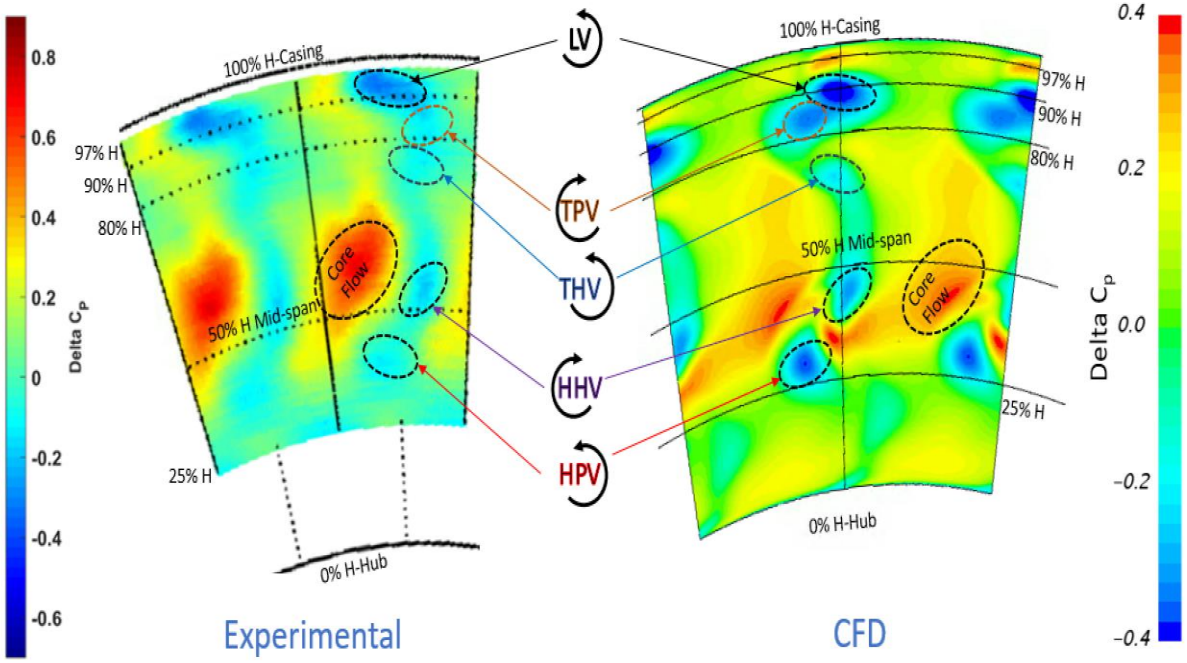


Figure 4-2 Pressure Contour Plots for Baseline Design

The passage vortex generated near the hub side is due to boundary layer interactions of the fluid flow with the blade and hub surface. It is called a Hub side Passage Vortex (HPV) and rotates in a CCW direction. Above the HPV, near the mid-span of the domain, HV generated is visible near the hub side. It is typically initiated close to the intersection of hub and blade leading edge. It then splits into the pressure side and suction side of the blade and propagates downstream in a radially upwards direction, as shown in Figure 1-3. The HHV that is generated after merging of the PSHV and SSHV can be observed near the hub side in the measurement plane. The HHV is rotating in the opposite direction of the HPV, i.e., in CW direction. Both HPV and HHV are the regions with reduced momentum in between the high momentum core flow regions. The HV near the tip side i.e. THV, is also visible in the CFD plots, rotating in CCW direction. However, the strength of tip side HV is less than the hub side HV.

The vortex of interest for this study is present near the blade tip, the one which leads to leakage losses in the rotor stage. As discussed before, the leakage losses can be governed by two vortex structures, Leakage vortex (LV) as well as the Tip-Passage vortex (TPV). The circular vortex structure closer to the casing is LV and just below it lies the TPV. It is difficult to differentiate these in the current experimental results, but their presence is validated by Maral [19]. The leakage fluid from the gap between the blade tip and the casing surface leads to LV. For the baseline case, as there are no modifications present on the casing surface, there are no flow interruptions due to any tip-mitigation schemes. Similarly, due to no change in pressure gradient, secondary flows such as TPV are unaffected. Thus, LV and TPV form the base of comparison for different casing designs. LV in the baseline case has lower values of delta $C_P$. Hence, the LV has a higher strength in comparison to TPV and other vortex structures too. The momentum deficit and losses due to LV are also higher in comparison to the other vortex structures. The LV is rotating in CCW direction near the blade suction surface at 90% and the TPV is rotating in CW direction near the 85% H.

Above the LV, due to the shearing effect of the casing surface, presence of the high momentum region can be detected. The shearing effect is due to relative motion between the rotating blade tip and the stationary casing surface. Around 97% H, the fluid flow in between the casing surface and the leakage flow have a higher-pressure value. This can be called “Scrapping Vortex” due to the shearing effect. This scrapping vortex is helpful in improving the performance of the turbine as it has a negative effect on the LV. Further, for casing designs, changes in the strength of Leakage vortex (LV) and Passage Vortex (PV) due to change in grooves designs on the casing surface is analyzed.

The pressure contour plots for the design of the spherical patterns are shown in Figure 4-3. Result obtained through experimental study is on the left and CFD results are presented on the right side of the figure. The range of delta $C_P$ is kept constant as the baseline plot to facilitate a better comparison. Spherical patterns do not provide any different characteristics for the pressure contour plots due to which the contour plots look similar to the baseline design. The vortex structures for the spherical patterns design have small strength variations when compared with the baseline design. The LV is a bit spread out and it is closer to the TPV and a slight increment in the strength of the TPV is also observed. Due to higher TPV strength, adverse effects are anticipated for such patterns. This would lead to increased losses near the 85% H region where the TPV is located. The HHV is also significantly extended in the wake region as compared to the baseline design. Near the casing surface, a reduced high momentum region can be observed due to reduction of the shearing effect. The presence of small cavities instead of a smooth surface reduces the surface contact area of the flow.

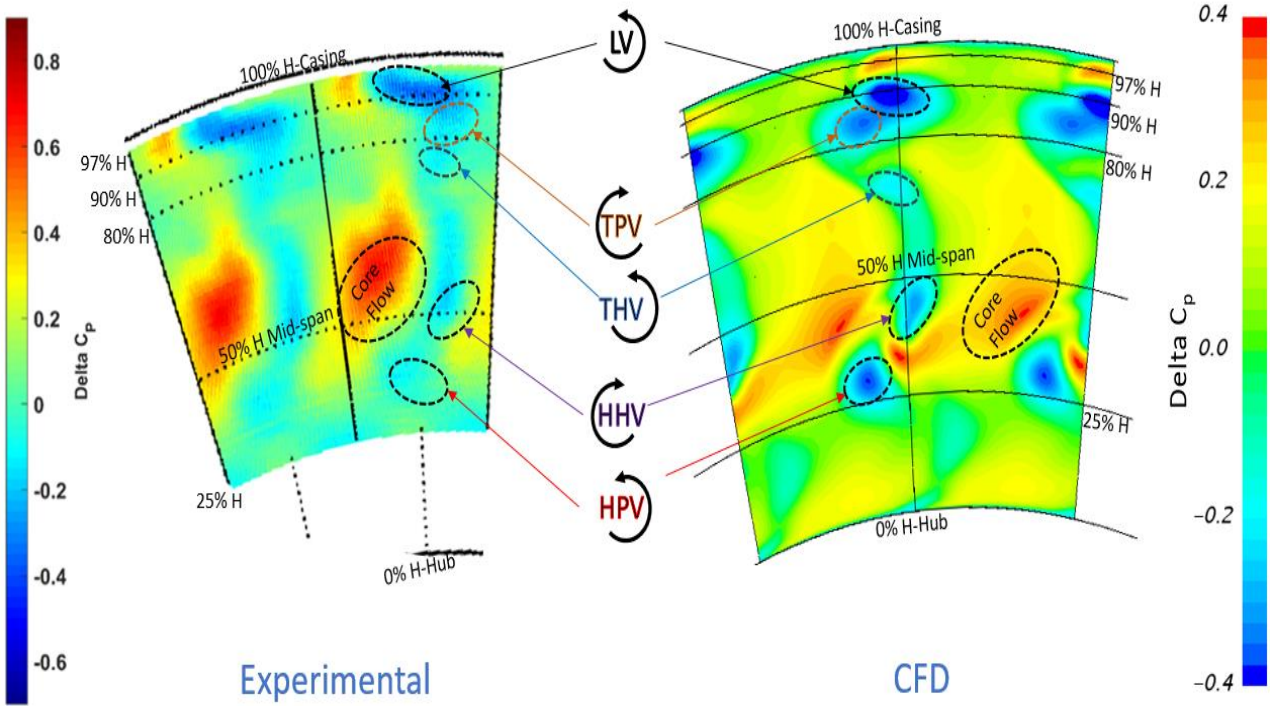


Figure 4-3 Pressure Contour Plots for Spherical Pattern Design

For axial grooves design, prominent variations in the pressure contour plots can be observed as compared to the baseline design and spherical patterns design. The pressure contour plots for the new casing groove design can be seen in Figure 4-4. In comparison to the baseline casing design, the LV near the tip is accompanied by the increase in the higher momentum zone (red zone) for axial grooves. The axial grooves provide high-velocity fluid into the suction side of the domain. The red area on the top is due to the high-velocity flow inside the grooves. The grooves provide a free path for the fluid and the ribs in between them have constrained space. The high momentum fluid from the grooves leads to the destruction of low momentum vortex structures. Also, due to the endwall of the grooves, accumulation of the fluid arises in this region, which then rolls into an additional vortex similar to scrapping vortex. This vortex can be visualized on the left side of the LV. The presence of this high total pressure coefficient zone leads to better rotor efficiency. The strength of LV is significantly reduced due to the presence of grooves in the direction perpendicular

to flow. The reduced strength of LV is visible in both experimental as well as CFD plots. The LV is shifted towards left, i.e., away from the suction side of the blade surface. The TPV is also diminished as it is entirely absorbed by the counter-rotating LV. The THV is also absorbed in the wake region as it not visible. As the modifications are done near the casing surface, there is no noticeable change below 60% span.

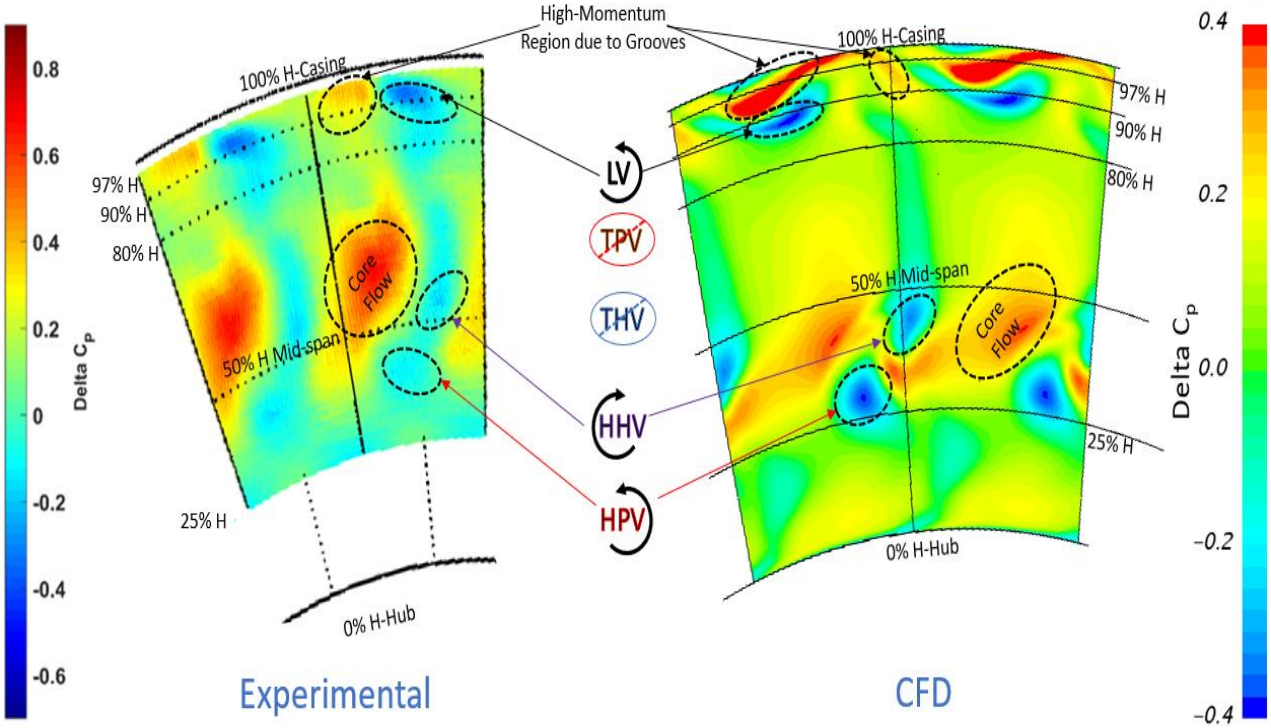


Figure 4-4 Pressure Contour Plots for Axial Grooves Design

Pressure contour plots for the circumferential grooves design shown in Figure 4-5, also illustrate variations of the vortex structures. The LV in this design has very low strength in comparison to the baseline and axial design. This movement of LV might be due to the presence of higher strength of TPV. The orientation of the grooves leads to minimal leakage flow. The circumferential grooves reduce the mass flow rate of leakage fluid passing into the suction side. Overall, the strength of the LV is reduced, but it merges with the TPV ahead and forms a higher strength TPV. There is also a

shift of the vortex away from the suction side of the blade along with an increase in the strength of TPV. An increase in strength of TPV leads to reduced efficiency near the 80% span but the LV is comparatively small and is also pushed downwards from the casing surface which leads to reduction of losses in the 90% region. In addition, the high momentum scrapping vortex is also absent for the circumferential grooves due to reduced fluid flow inside the grooves. THV is displaced marginally below in spanwise direction and the rest of the vortex structures below 60% span are similar to the baseline and other designs. Overall, the LV for the baseline, axial as well as spherical design is present at an almost similar location with similar strength when compared with experimental plots respectively.

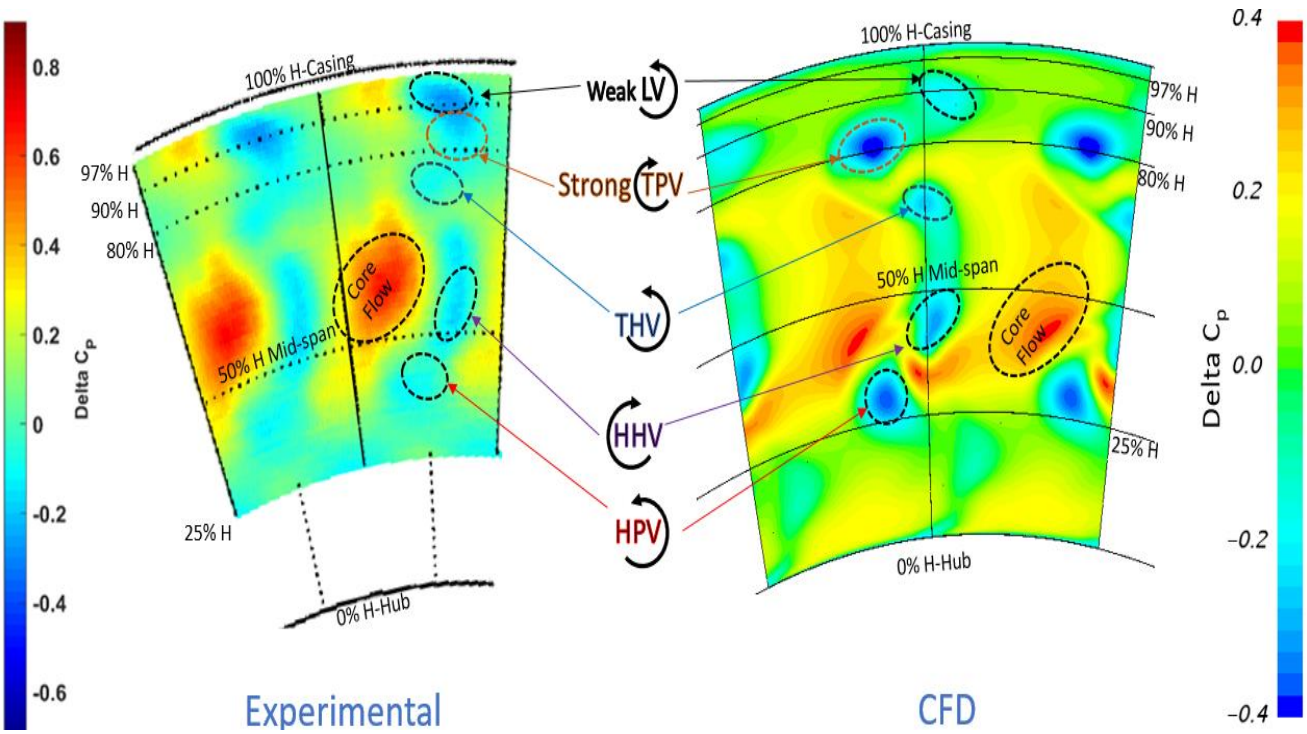


Figure 4-5 Pressure Contour Plots for Circumferential Grooves Design

The spanwise distribution of delta $C_P$ for a new design and baseline design is shown in Figure 4-6. Data shown is from 25% to 100% span, to visualize the casing effects. The delta $C_P$ values shown below are the passage average of the delta $C_P$ at each radial location. For the baseline design, the minimum value of delta $C_P$ is at 90% span where the center of leakage vortex resides. The maximum value of delta Cp is at 45% span i.e., near the core region. All other vortex structures lie in between these two extreme points. Small negative effects present in the curve is due to the secondary vortices like PV and HV. The pressure contour plots for baseline design shown in Figure 4-2 corroborates the spanwise location of each vortex. This plot is very useful in visualizing the effect of new tip leakage mitigation designs in comparison to the baseline design. The baseline design is used as a reference to compare all designs. Thus, the delta $C_P$ curve, which lies on the right side of the baseline curve, leads to comparatively higher total pressure leading to improved performance. The left side of the baseline curve indicates a deteriorating performance. The improved performance region is denoted with green lines and yellow lines are used to denote the deteriorating zone. From Figure 4-6, above 80% span, improved performance is observed for the "New_Design". However, some detrimental effects can be observed below the 80% span due to the interaction of vortices with the core region.

Further, the circumferentially averaged delta $C_P$ values can be used to calculate the Figure of Merit (FOM). FOM is the most efficient way to numerically represent the performance of low-speed cold flow turbines like AFTRF. Graphical markings of the regions in Figure 4-6 helps in the calculation of Figure of Merit for the Tip region which is from 70% to 97% span. On the right side of the figure, a dotted line parallel to the y-axis is present which denotes the maximum delta $C_P$ value for the Baseline Area. This dotted line is used to calculate the Baseline Area, $A_B$, and Passage i Area, $A_i$. The area between the dotted line and the delta $C_P$ curve for baseline design denotes the baseline Area, $A_B$ and the area between the dotted line and the delta $C_P$ curve for "New_Design" denotes

the Passage i Area, $A_i$. The difference of the Baseline Area, $A_B$, and Passage i Area, $A_i$, is normalized using Baseline Area, $A_B$, to calculate FOM values. This FOM expression is indicated in Equation 4-3. Thus, positive values of FOM indicate the improved performance of "New_Design" in comparison to the Baseline Design. Detailed discussion for FOM calculation can be found in [8] by Andichamy.

$$Figure\ of\ Merit, FOM\ = \frac{A_B - A_i}{A_B}$$

.....Equation 4-3

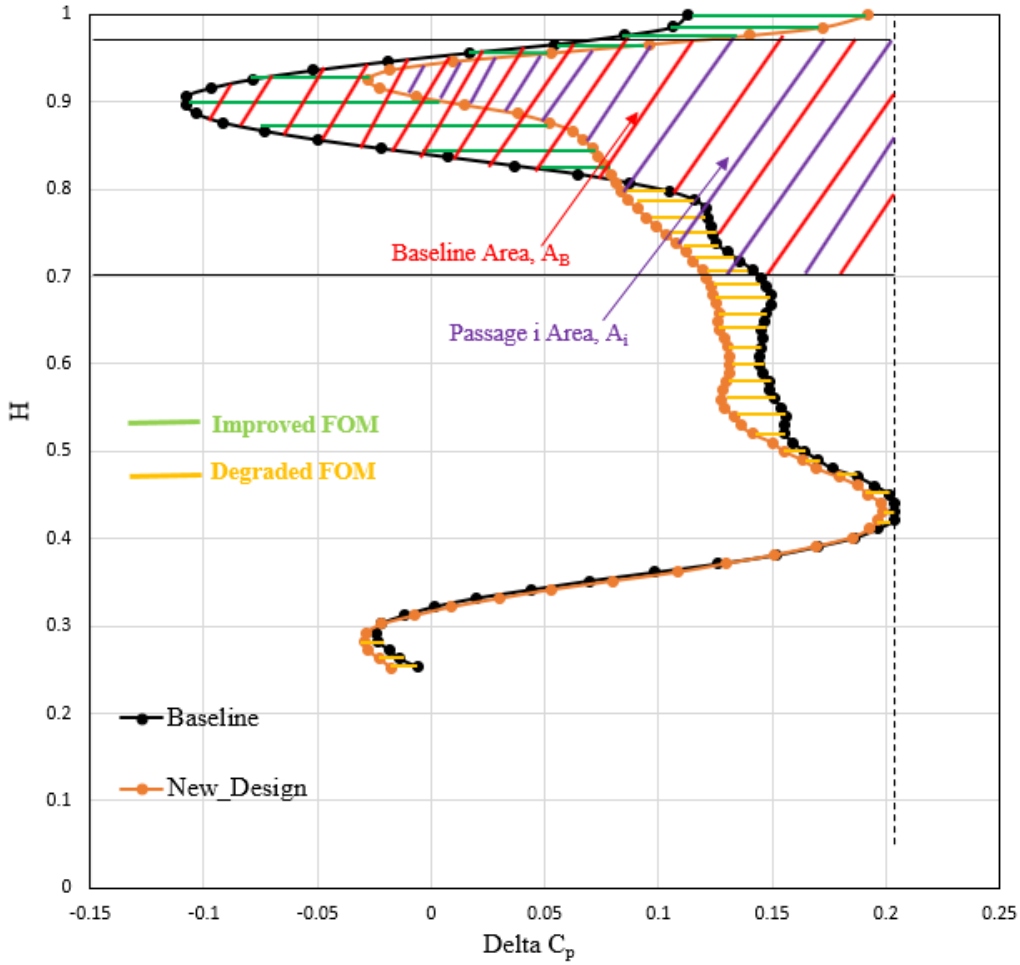


Figure 4-6 Spanwise Distribution of Delta $C_P$ for Baseline and a New_Design

The delta $C_P$ plot for all three modified casing designs and the baseline design is illustrated in Figure 4-7. The trend of the delta $C_P$ plot obtained using the experimental values is similar to the curve obtained from the computational study. From the observation of experimental and CFD results, below 60% span, there is a negligible change in delta $C_P$ for any of the modified design with respect to the baseline design. This is justified by the core flow region in pressure contour plots, which is not changed significantly for the new designs. In the tip region, variations in the vortex structures because of grooves can be observed. The delta $C_P$ plot shown in Figure 4-7 is from 60% to 100% span. This truncation of span leads to a detailed visualization of the changes near the tip region due to different casing modifications.

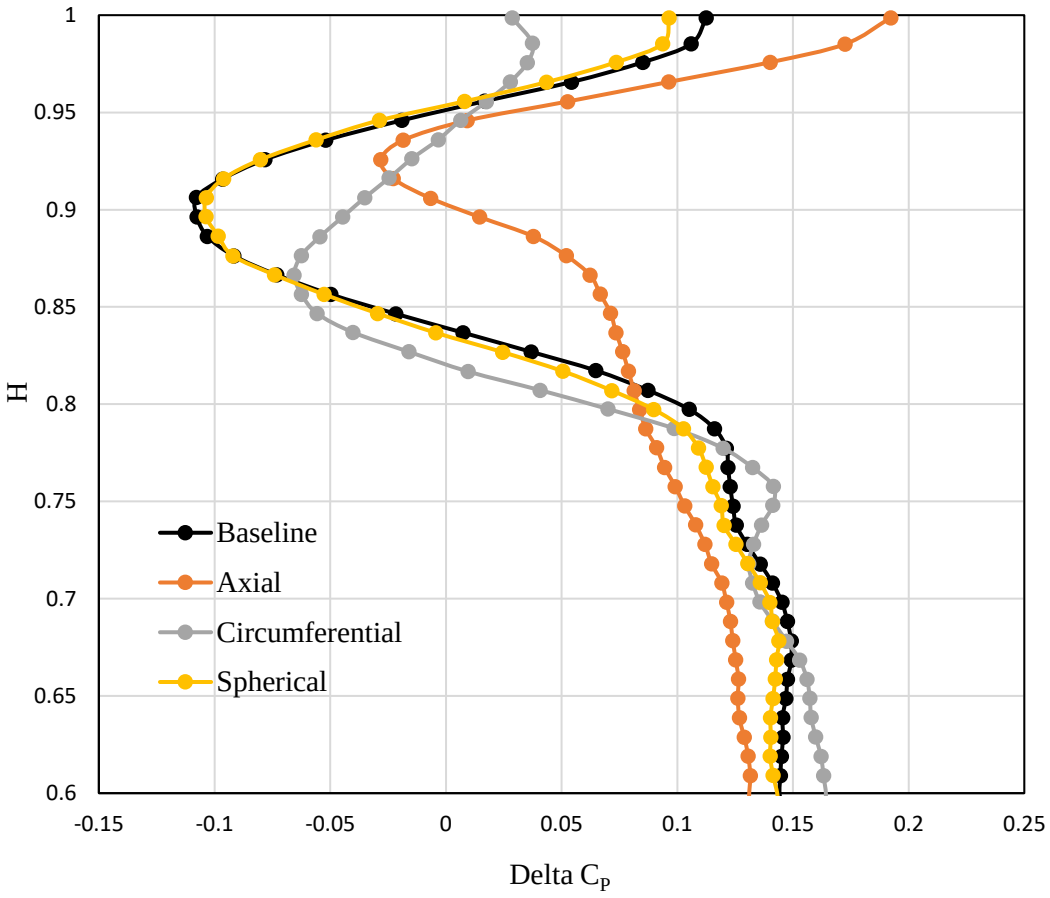


Figure 4-7 Spanwise Distribution of Delta $C_P$ near the Blade Tip-Region

For spherical pattern design, the delta $C_P$ curve shown in Figure 4-7 is similar to the baseline model. In fact, it is overlapping with the black curve of the baseline design for most of the regions. However, there is a slightly negative effect below the 85% span and above 95% span. As observed from pressure contour plots in Figure 4-3, the leakage vortex and tip-passage vortex for the spherical pattern design is at the same location as baseline design. However, the strength of TPV is slightly higher in comparison to the TPV present in the baseline design. Also, the high momentum region above 96% span is reduced due to the presence of spherical patterns.

In the case of axial grooves design, as discussed, the presence of a higher momentum region near the tip (94% to 100% span) leads to very high positive values of delta $C_P$ in this region compared to the baseline model. Also, below the region, a positive effect on the pressure data can be observed due to reduced strength of LV. The center of leakage vortex is shifted to a 93% span in comparison to the leakage vortex of baseline design which is at 90%. The absence of TPV for the axial design is justified by the lack of negative values of delta $C_P$ from an 80% to 90% span.

Circumferential grooves design has a positive effect above 86% of span due to reduced LV strength. In fact, LV is so highly diminished in the region of 91% to 94% that it achieves higher delta $C_P$ value than the axial design in that region. There is a slight decrement in delta $C_P$ values above 95% as circumferential grooves tend to eliminate the higher-pressure zone near the casing surface. A higher strength of TPV is evident near the 85% span as the values of delta $C_P$ are less than the respective values for baseline design. Therefore, the circumferential design has mixed performance; less efficient as compared to axial design but marginally better than the baseline design. The grooves orientation leads to a reduction in free movement of leakage flow towards the suction side.

Table 4-1 shows the FOM values calculated for the tip region. The tip region is defined as the interval from 70% to 97% blade span. This tip region was selected as it is comprised of the essential tip-side vortex for all the designs. It can be seen that Tip_FOM values presented in Table 4-1 are close to the experimental values. This comparison helps to assess the CFD results in numerical terms. Overall, the Tip_FOM value for axial design is 20.8%, which proves the benefit axial grooves possess. Axial grooves provide the best Tip_FOM results as it leads to reduced leakage vortex strength and production of high momentum regions near the casing surface. Circumferential grooves, on the other hand, have positive effects due to the elimination of LV but the effect is reduced by the negative strength of TPV. It has a Tip_FOM of 3.1% for the CFD results and 3.9% for experimental data. However, spherical pattern results in a negative Tip_FOM value of -3.6%. This shows that the current design of spherical patterns leads to deteriorating performance due to the increased TPV strength. It should be noted that uncertainties for total pressure measurements were $\pm$5Pa [15]. The detailed uncertainty analysis for the AFTRF can be found in Andichamy [8] [26] and Doshi [15].

Table 4-1 Tip Figure of Merit (FOM)

| **Design** | **Tip_FOM (70 to 97% Span)** | |
|---|---|---|
| | **Experimental** | **CFD** |
| Spherical Patterns | -3.7% | -3.6 % |
| Axial Grooves | 19.4% | 20.8 % |
| Circumferential Grooves | 3.9% | 3.1 % |

### 4.2 Flow Physics Analysis Based on Contour plots

Streamline visualization study is one of the best ways to understand the three-dimensional nature of the flow as it depicts the vortex interactions and flow structures. The streamlines for all the three preliminary casing designs along with the baseline design are shown in Figure 4-8, wherein, seeding of streamlines is from one constant source i.e., from the pressure side of the blade tip. This type of seeding source was used in order to analyze the flow leaking through the blade tip gap. The streamlines plot for the baseline case is shown on the top left of Figure 4-8. It displays two different vortex structures, TPV and LV. The LV is gathering most of its strength from the fluid leaking from 30% of the axial chord to the trailing edge of the blade. When the flow passes from PS to SS of the blade, it tends to follow a direction that is mostly perpendicular to the blade's camber line. This leakage flow forms the LV, which tends to roll in the counterclockwise direction. Different colors of the streamlines represent the velocity magnitude of the fluid. The LV has very high velocity as compared to the TPV, which is due to the rotational motion of the blade. The TPV gathers most of the fluid from the leading edge of the blade and the leakage flow downstream. The TPV moves towards the suction side of the blade as it tends to roll into a clockwise vortex. This vortex tends to increase its size as it moves downstream. However, it loses its energy causing a momentum deficit in that region. The leaking fluid, which does not contribute to the LV, merges with the TPV, eventually leading to an increase in the diameter of TPV downstream. The location of TPV and LV are consistent with the experimental results, and more information related to these secondary structures can be found in [11] [19] by Kavurmacioglu and Maral.

For the design of spherical patterns, streamlines plot can be visualized on the top right side of Figure 4-8. For this design, based on the visual comparison, LV and TPV are at a similar location as in baseline design. However, there is a slight increase in the strength of the TPV, which results in lower FOM.

The streamline plot for the design of axial grooves is present in the bottom left of Figure 4-8. From the figure, it can be observed that TPV is almost negligible in size. Also, it tends to merge with high momentum LV downstream. Near the trailing edge of the blade, it can be seen that the flow and grooves direction are aligned with each other. The LV in the axial case is formed by two vortices, one generated from the fluid flowing inside the grooves and the other is generated in the ribs between the grooves. The fluid flow from the grooves has a very high velocity which results in pushing the LV away from the SS and also leads to a reduction in the momentum deficit region generated by the LV. Overall due to the reduced LV strength and elimination of TPV, there is increased efficiency in axial grooves design.

Circumferential grooves are aligned in the direction which is almost perpendicular to the flow direction. This orientation obstructs the flow to pass freely into the suction side, which helps to reduce the leakage mass flow rate. The streamlines plot for the circumferential design in the bottom left of Figure 4-8 reveals that LV cannot be formed completely. Moreover, due to the obstructing pathway for the leakage flow, it loses most of its momentum, resulting in very low-velocity flow deposited into the suction side. This flow when merged with the TPV, there is an increase in its strength and creates a very high momentum deficit region below the LV. The TPV is pushed marginally below compared to baseline design due to the increased amount of flow merged into it from the LV. The reduction in LV is suitable for a higher performance near the tip but below LV, the increased TPV leads to a negative effect.

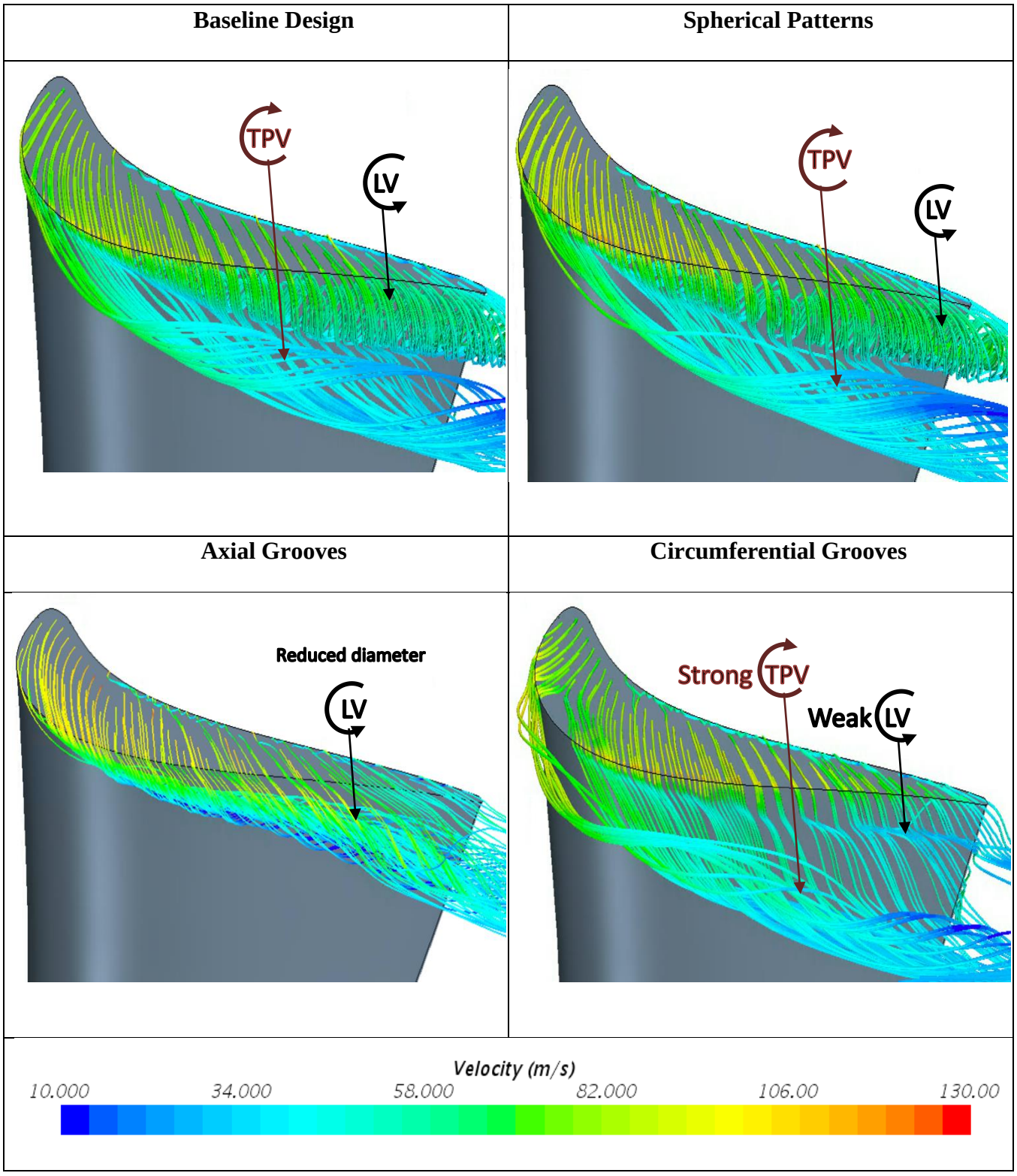


Figure 4-8 Velocity Streamlines Plot for Tip-Leakage Analysis

Wall shear stress on the suction side of the rotor blade and its tip surface are shown in Figure 4-9. These shear stress plots are useful in visualizing the presence of vortex structures and flow on the blade tip. The black line shown on the plots is to denote the mid-span of the blade for all casing designs. The low shear stress regions (below 10 Pa) represents separation zones. These regions are momentum deficit regions due to low-velocity gradients. Such regions provide approximate locations of different vortices such as LV, TPV, THV, HHV and HPV which can be seen on the suction side. The high shear stress regions (above 30 Pa) are present near the blade mid-span and some parts of the blade near the tip and hub surface. These regions represent high momentum flow due to the presence of a higher velocity gradient.

The core flow region near the blade mid-span for all designs are similar in terms of strength and location while vortex structures differ owing to different characteristics of each design. There are minute variations in the plots for spherical patterns in comparison to the baseline design. It can be observed that the LV and TPV in spherical patterns are slightly spread out in contrast to the baseline design. In the baseline design, the high shear stress zone is present between LV and TPV. However, for spherical patterns, these regions are present at intermittent locations due to the increased strength of TPV. The remaining vortex structures near the hub (HHV, HPV) and tip (THV) are unaffected. On the blade tip surface, a reduced velocity gradient region near the blade leading edge can be observed. This reduced velocity gradient was also observed by Rao [10] while performing experimental research on AFTRF using oil flow visualization. In spherical pattern design, there is an additional flow inside the hemispheres, which creates an impingement effect and results in an increased velocity gradient and flow recirculation. This specific flow pattern leads to a higher shear stress region in circular form on the tip surface of the spherical patterns design. It can be predicted that by increasing the number of hemispheres, there might be a reduction in low shear stress regions. However, there can also be an adverse effect due to the increase in TPV strength.

The shear stress plot for axial grooves design shown on the bottom left of Figure 4-9, exhibits many variations in comparison to the baseline design. First, the strength of LV is reduced. Second, the streamlines plot showed that the LV has moved away from the SS, and hence, the flow close to the suction side of the blade is not affected. Below the LV, there is a very high-velocity gradient on the blade surface. Next, due to a very high shear stress region, the TPV growth is greatly restricted. All other hub side vortex-like HHV and HPV is unaffected by the axial grooves. THV is located at a higher span location near the trailing edge along with reduced strength in comparison to other designs. On the tip surface of the blade, a high shear stress region is present below the grooves. Due to the presence of constrained space in the ribs and very high mass flow rate allowed by the direction of the grooves, the velocity gradient is steeper on the blade tip surface in comparison to tip surface for the baseline design. The effect of a higher velocity gradient is also visible near the leading edge of the blade. The intermittent high (in the red or yellow shade) and low shear stress regions (in the blue shade) on the blade tip characterize the increased amount of flow inside the grooves and decreased flow rate inside the ribs.

For circumferential grooves design, the shear stress is low for most of the regions on the blade tip surface. Near the leading edge of the blade, streaklines due to shear stress show the orientation of the grooves and the low momentum fluid passing through it. Two perpendicular low shear stress lines on the blade tip are observed around 50% axial chord. One streakline is oriented in the direction of the grooves whereas the other is perpendicular to it, representing the fluid leaking between the blade tip and casing surface. On the suction side, it is observed that the leakage vortex has reduced its strength by passing the low-velocity fluid into the TPV. This explains the reason for an increase in the TPV for the design of circumferential grooves. There is also an increase in the shear stress at an intermittent location in between the LV and TPV. All other vortex structures are similar to baseline and spherical design.

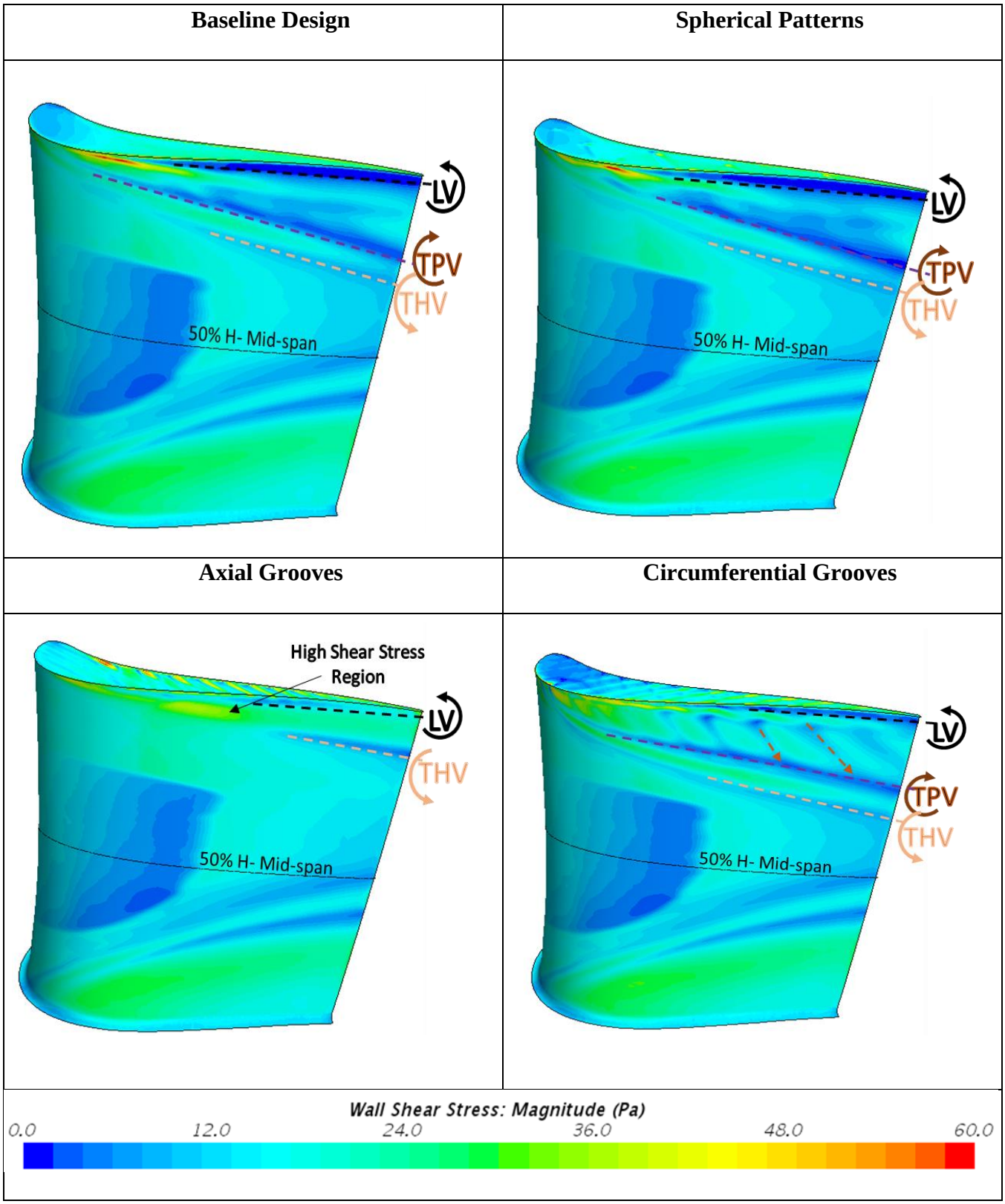


Figure 4-9 Wall Shear Stress Contour plot on the Tip Surface and Suction Side of Rotor Blade

Figure 4-10 represents the shear stress on the rotor casing surface for the three casing designs and the baseline design. The view is captured from outside the rotor and hence, the blade tip surface is not visible from this side. However, the contours of shear stress are helpful in locating the approximate blade tip surface. For the baseline design, higher shear stress can be seen for the casing surface just above the blade tip. The rest of the casing has very low shear stress due to open flow passages for the fluid. The reduced space between the blade and the casing surface leads to higher shear stress. The red portion on the blade tip is near the pressure side, which represents the bubble formation on that side. This red zone is also visible in the spherical case. For the design of axial grooves, the red region is intermittent. The red zone is evident in the constrained space between two grooves called ribs, while within the grooves, the shear stress is reduced due to more space between the casing and the blade tip surface. This high shear stress region is missing in the circumferential design, leading to the conclusion that there is a reduction in the amount of flow passing through the tip gap. As the grooves are oriented in the tangential direction of the flow, the flow rate gets reduced, leading to reduced shear stress.

Behind the red zone, there is a separation line which extends until the trailing edge of the blade for the baseline design. A similar separation line can be observed for the spherical case, with a broken region in some spots due to the presence of spherical patterns close to it. However, this separation line is missing in axial grooves design and diminished in the design of the circumferential grooves. One of the reasons for less separation in the axial design can be attributed to higher velocity produced due to the grooves. Finally, for the circumferential case, due to less momentum fluid throughout the region, the separation line might be concealed along with the low-velocity areas.

Most importantly, from the start of the axial grooves ahead of the blade leading edge, there is a sudden increase in the wall shear stress. However, with the onset of the circumferential grooves, there is a decrease in the wall shear stress to a low level. This reduction can be attributed to the orientation of the grooves; with axial grooves aligned close to the flow direction, helping the flow to continue in the same direction. There is a very high mass flow rate due to this orientation of the grooves near the blade trailing edge. This high mass flow rate of the fluid imparts some energy into the LV that is generated. Since the grooves are almost aligned with flow direction, there is less loss of momentum and very high velocity on the suction side. The axial grooves tend to conserve the velocity of the flow to a great extent. However, near the blade leading edge, axial grooves orientation is in such a manner that there is a maximum obstruction for the leakage.

In the case of circumferential grooves, wall shear stress contour plots have different velocity gradients. For the circumferential case, it is observed that as the fluid gets into the grooves, there is a reduction in the velocity. Behind 30% axial chord, the flow momentum is lost in this case due to the alignment of grooves in the almost perpendicular direction of the flow. As the fluid tends to turn into the direction of the grooves, there is a considerable loss of momentum. When the flow reaches the suction side, the flow speed decelerates, leading to reduced LV. However, near the blade leading edge, a high shear stress region is observed near the suction side in comparison to the axial design. This conveys that such grooves are not helpful near the blade leading edge as it increases the secondary losses in this region. This eventually leads to an increase in the strength of TPV.

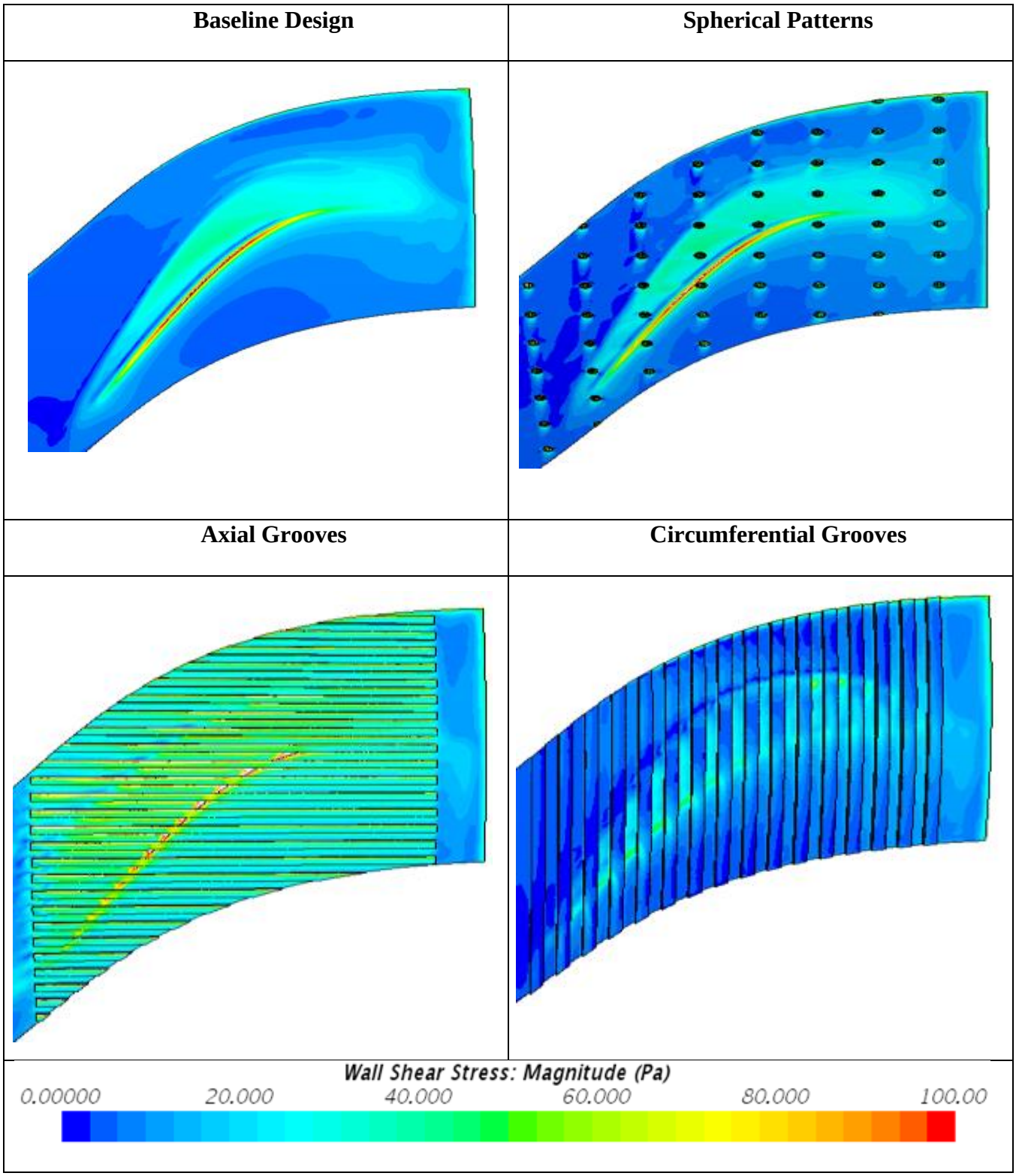


Figure 4-10 Wall shear stress contour on the casing surface

As discussed before, the axial grooves lead to the generation of higher momentum zone, while circumferential grooves lead to momentum deficit region. This fact can be better understood by the velocity contour plots present in Figure 4-11. The velocity profile is shown on a plane connecting the blade tip and casing surface on the suction side of the blade. Inside the axial grooves, a high momentum zone can be seen, which is pushed into the suction side of the blade. The axial grooves act as a high energy ejector system working in the rotor to provide an additional performance benefit. Although the higher velocity leads to a higher mass flow rate between the casing and the blade tip surface for the axial design, work is done on the fluid in this region, which prevents it from forming a momentum deficit region. Inside the circumferential grooves, there is low-velocity flow leading to a very low momentum region. This is helpful to reduce the leakage rate, but it does not act as a beneficial design due to the abolition of the higher momentum region. The spherical patterns do not show much difference with respect to the baseline case. The spherical patterns are shorter cavities developed to disturb the flow at regular intervals. The circumferential grooves design, as seen, can block the leakage flow, which passes over the blade tip surface while the axial grooves can provide a path for the leakage flow.

All these flow visualization plots form an essential understanding of the improved design. It can be concluded that the orientation of grooves direction plays an important role with respect to the leakage flow and secondary losses. Axial grooves proved to help eliminate the TPV and move the LV away from the SS of the blade. The presence of a high momentum region increased the LV strength compared to circumferential design. The circumferential grooves are useful in reducing LV, but it increases the TPV due to its orientation near the blade leading edge. Also, as circumferential grooves are not aligned in a direction perpendicular to the flow, the grooves from 30% to 100% axial chord need to have an angle of 90 degrees with respect to the flow direction observed. This could help in reducing LV as well as the TPV.

| Baseline Design | Spherical Patterns |
|---|---|
| 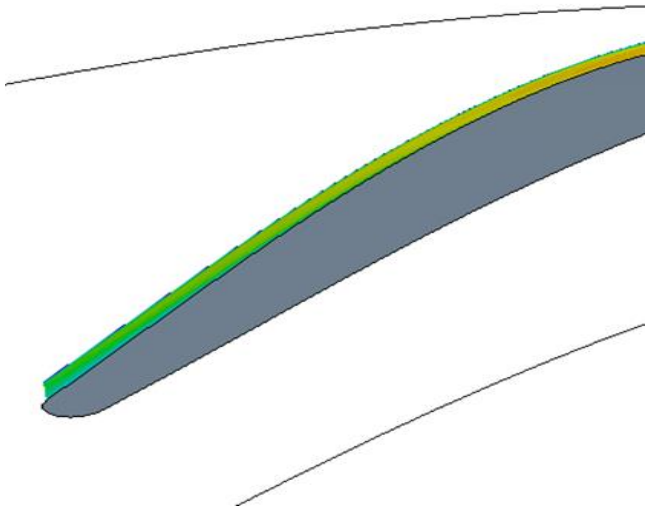 | 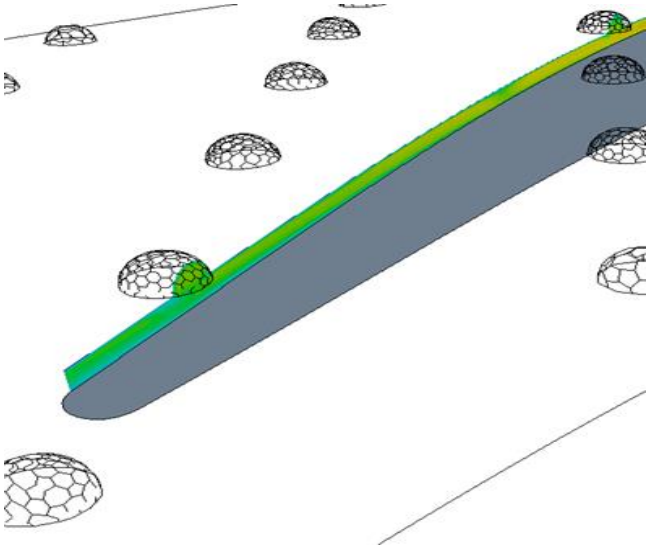 |
| **Axial Grooves** | **Circumferential Grooves** |
| 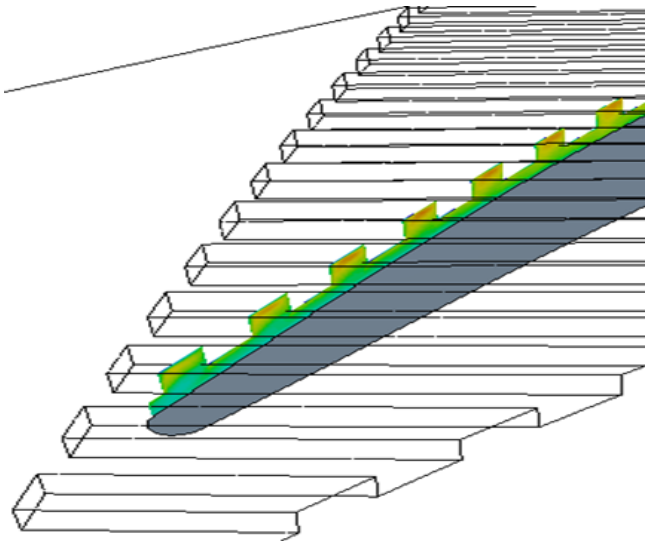 | 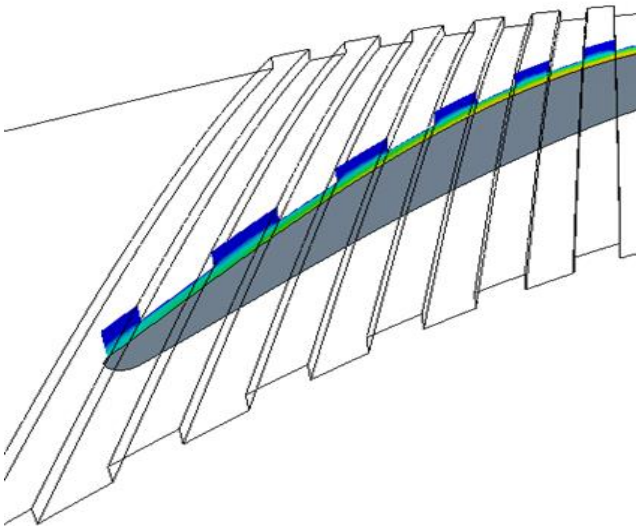 |

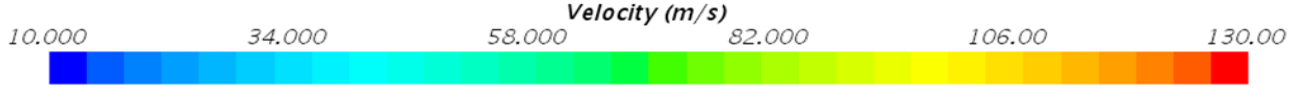


Figure 4-11 Velocity Contour Plots on Suction Side of Blade in between blade tip and casing surface

# Chapter 5

## An Improved Casing Groove Design: Camberline Grooves

Based on the preliminary casing pattern design studies, an improved version of casing grooves design was developed. As discussed in the previous chapter, the vortex structures generated for the design of the spherical patterns had minor strength variations. Thus, the spherical patterns did not produce many changes in comparison to the baseline design. The axial and circumferential grooves proved to be major factors in improving the performance compared to the baseline design. Thus, the two designs had many design features that influenced the new improved design. It is observed that the design of axial grooves almost eliminates the passage vortex. The circumferential grooves design reduces the tip leakage vortex. In order to improve the turbine efficiency, there is a need to reduce both leakage vortex as well as tip passage vortex. Thus, contributions from these two design studies were prominently utilized. The blade tip shear stress profile was also helpful in understanding the flow angles near the tip surface. Near the blade leading edge, i.e., from 0 to 30% blade chord, leakage flow is nearly perpendicular to the axial grooves. From the streamlines plot of axial grooves design, it is observed that the axial grooves impinge the flow in this region and hence reduces the dissipation of the passage vortex to a higher strength downstream of the blade. The circumferential grooves in this region do not provide aid in obstructing the flow. However, in the downstream region, the circumferential grooves obstruct the flow to a greater extent, which leads to a great momentum deficit of tip-leakage vortex. As the grooves are not aligned perpendicular to the flow direction, this leads to the low momentum fluid merging with the passage vortex and increases its strength. Hence, the profile of the grooves at a particular angle in the region beyond the 30% axial chord region would be beneficial. Considering all these factors and the fact that the blade surface is curved, the optimized groove shape was chosen. Ultimately, grooves

parallel to the blade camber line were developed, as shown in Figure 5-1. The improved casing design is named as “Camberline Grooves.”

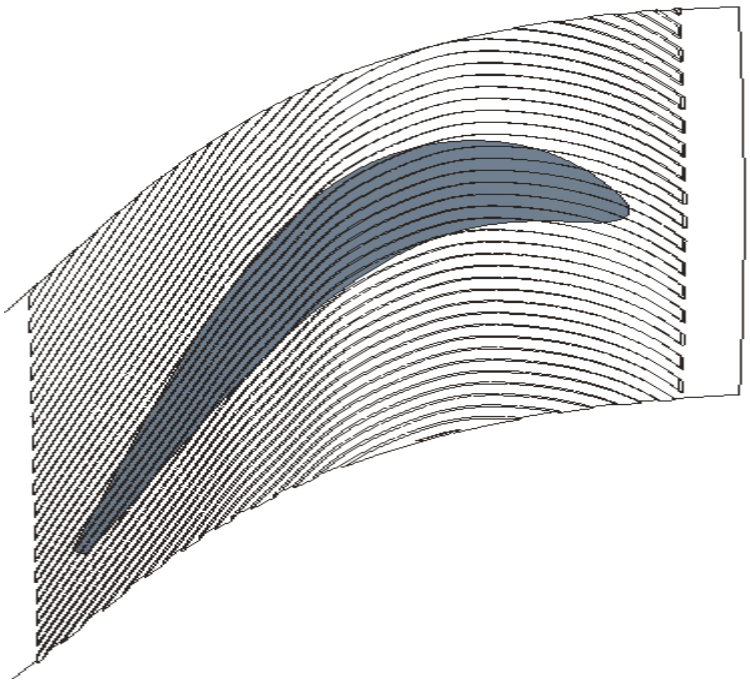

Figure 5-1 Geometry of Camberline Grooves Design

The new camberline grooves design has similar dimensions to the design of the axial and circumferential grooves. The width of the grooves is 3mm with even spacing of 3 mm to have a better comparison with different designs. The profile shape of the grooves is approximately parallel to be the camber line of the airfoil shape of the rotor blade tip.

The simulations were performed with the same boundary conditions and physical modeling equations. The measurement plane was also kept at the same distance, i.e., 25.4 mm from the rotor blade trailing edge. The pressure contour plots extracted at the measurement plane is shown in Figure 5-2. The contour plot obtained for camberline grooves design is shown on the right side and that for the baseline design is indicated on the left. Near the 97% span, a region close to the rotor

casing surface, there is the presence of high momentum fluid. The high momentum fluid has a higher strength for the design of camberline grooves in comparison to the baseline design. This shows that the grooves result in positive work on the passing fluid. Near 90% H, the presence of the LV is seen. The strength of LV for the baseline design is higher than that of the camberline design. The LV in the camberline design is somewhat dissipated and also pushed below along with left movement i.e., away from the suction side of the blade. It can be said that the leakage losses near the blade tip surface are reduced due to the new design. In between 80-85% H, passage vortex is visible, which is rotating in the opposite direction of LV, i.e., in CW direction. The strength of passage vortex is also diminished in the case of camberline grooves design. The growth of passage vortex is obstructed near the blade leading edge region due to the presence of grooves perpendicular to the flow direction. Since the measurement plane is downstream of trailing edge, the wake region is visible from nearly 40% to 80% H. Near 70% H, a small Tip-side Horse Shoe Vortex (THV) is visible which is generated due to the leading edge near the tip region. The THV is rotating in the CCW direction, and it represents the final merged structure of PS-HV and SS-HV. The THV in camberline design has comparatively higher pressure as compared to the baseline design, and hence, less momentum deficit in this region. Below 70% H, the contour plots are similar. Thus, the effect of the grooves is limited near the casing surface, from 70% to 100% H. In Figure 5-2, other vortex structures are also visible. Just below the 50% H, Hub-side Horse Shoe Vortex (HHV) is visible, which, as the name suggests, is generated due to the hub surface and the leading edge of the rotor blade near the hub side. The HHV has a CW direction of the vortex, which is in the opposite direction of THV. The secondary flows near the hub side boundary layer generate a hub side passage vortex (HPV), which is also opposite to TPV. Both hub side vortices, THV, and TPV for the camberline design are similar to the one in the baseline case. The high momentum region is the core flow, which is unaffected by the boundary layer and possesses higher kinetic energy. The region of core flow is similar in both profiles.

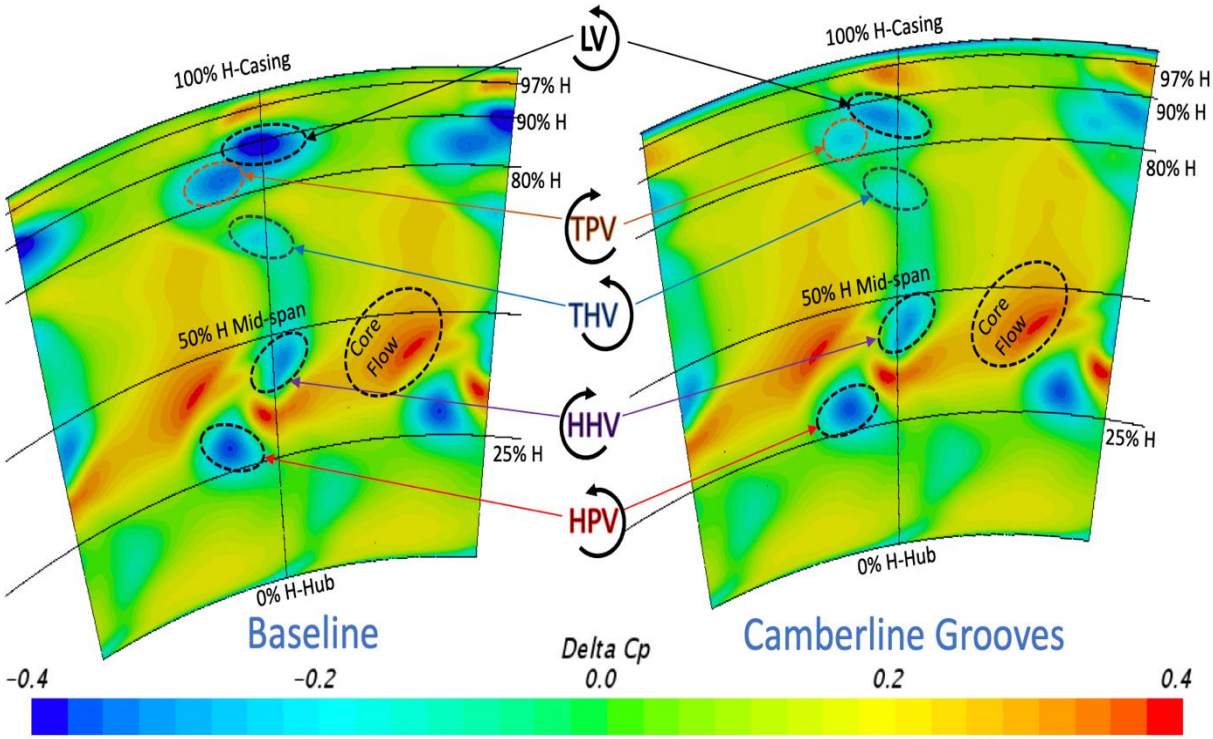


Figure 5-2 Pressure Contour Plots at Measurement Plane

A delta $C_p$ plot in the spanwise direction was generated for the new design, as shown in Figure 5-3. This figure depicts clearly, picture of the higher momentum region and momentum deficit region in comparison to the baseline design. The higher the delta $C_P$ values, the better is the performance of the rotor as it relates to the pressure rise in that section. Usually, near the 90% span, the LV leads to the reduction of delta $C_P$ values but the new camberline grooves shape reduces the leakage vortex strength. The highest value of delta $C_P$ corresponds to the center of the core flow region, which occurs at nearly the same distance for both the configurations. Below 70% height of the domain, delta $C_P$ profile for both configurations is similar, as observed in the contour plots as well. Near 75% H, there is a slight rightward shift of the camberline curve towards lower delta $C_P$ value due to the momentum deficit generated by the THV. However, camberline-shaped grooves still perform better than the baseline design. The delta $C_P$ values go on reducing from 75% to 90% span due to

the presence of Passage vortex and Leakage vortex. However, the drop in delta $C_P$ values for the baseline case is more pronounced than the design of camberline shaped grooves. Near the casing surface, the camberline grooves provide negative performance, which might be due to the wake effect generated by the grooves. Overall there is an improved performance region for the camberline grooves when compared to the baseline design.

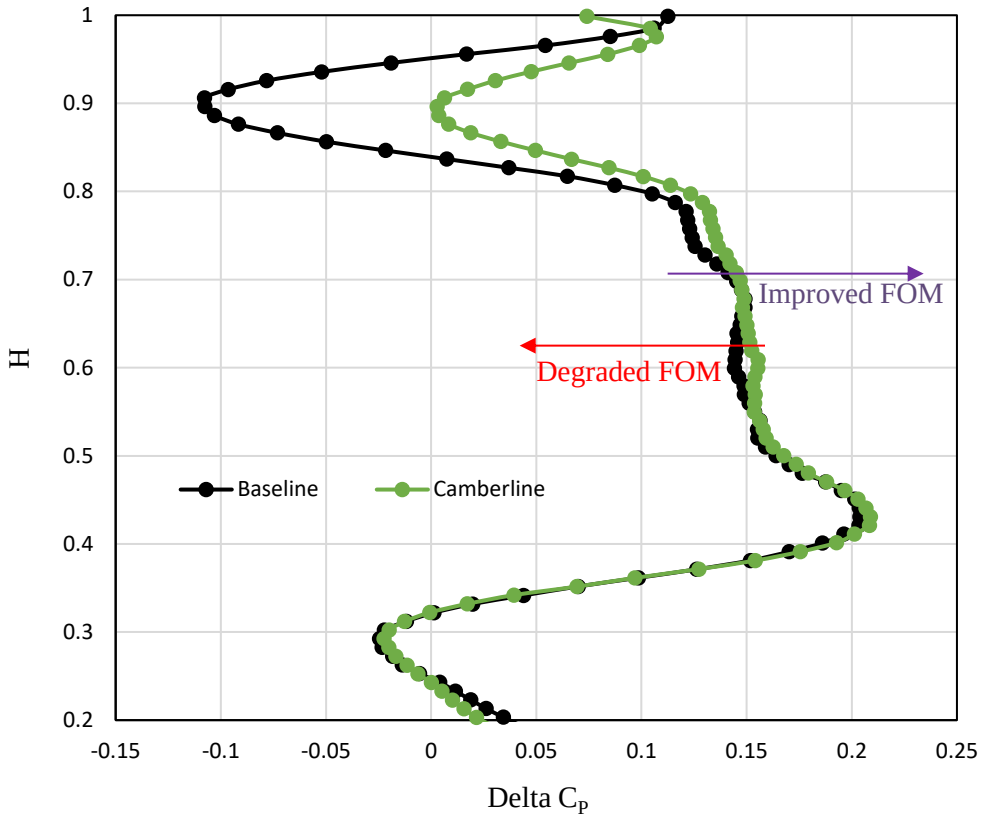


Figure 5-3 Delta $C_P$ Plot in the Spanwise Direction

Another useful parameter to compare the performance is the FOM value. The tip FOM value, i.e., FOM value for 70% to 97 % H, for the new camberline shape design, is 30.7%. This high FOM value proves that the current concept is a relatively efficient design in comparison to the baseline design. Also, this design is an improvement over all the three design modifications considered as it has a higher FOM as compared to the other three designs.

Streamlines for the camberline and baseline design are shown in Figure 5-4. The velocity magnitude color bar denotes that the blue colored streamlines have a very low velocity of around 30 m/s or below. The green hue is around 60 m/s, which is close to the velocity of rotor blades i.e., 54.04 m/s. The yellow and red streamlines near the blade tip surface represent a very high velocity of around 100 m/s. In comparison with the baseline design, it is observed that TPV, which is below the LV in the baseline case, is almost negligible. In fact, there occurs a significant interaction between the TPV and LV, which results in high energy dissipation of the leakage vortex, and thus a very low velocity. The LV, rotating in CCW direction, for the baseline design has a much higher velocity of around 60 m/s, in comparison to the LV generated for the new design which is around 80 m/s. LV and TPV are rotating in the opposite direction and, most importantly, are close to each other in the camberline grooves design, which leads to a reduction of the leakage vortex strength.

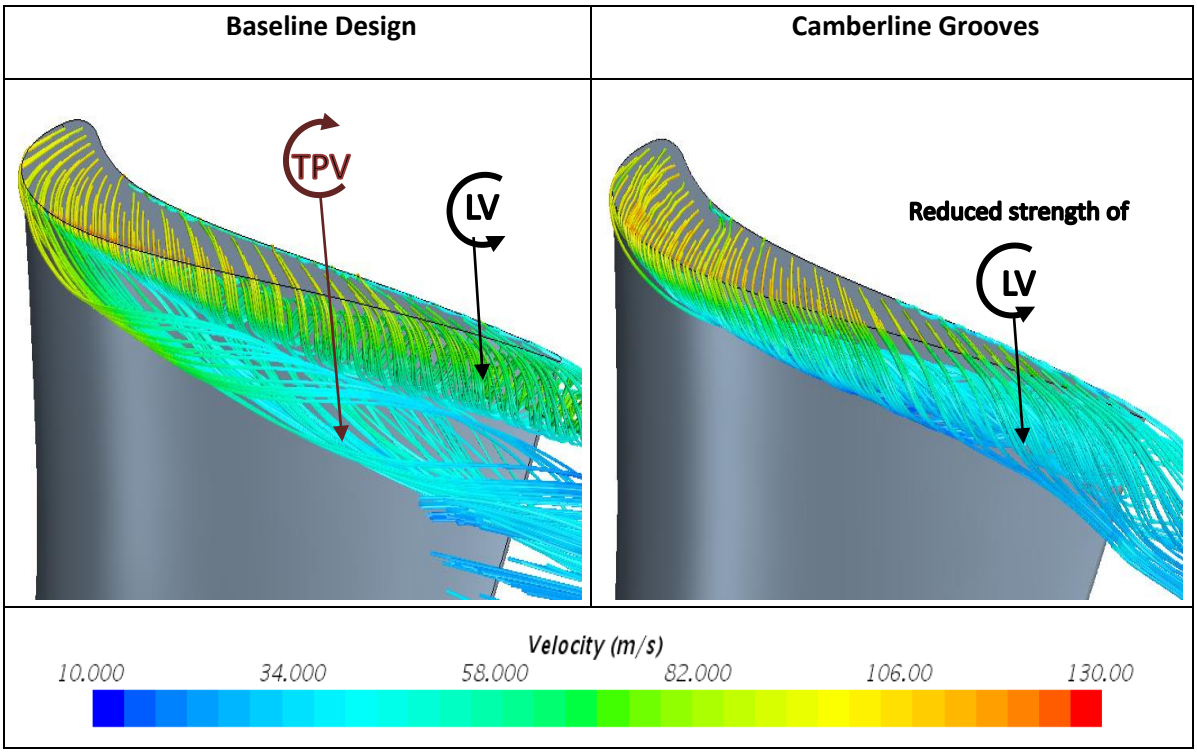


Figure 5-4 Velocity Streamlines Plot

In the wall shear stress contour plots shown in Figure 5-5, each of the vortex structures can be observed on the SS of the blade. The vortex structures near the tip (THV, TPV) for the new design are reduced to a great extent whereas there are no visible effects on the vortex near the hub side, i.e., HHV and HPV. The strength of LV is also reduced compared to the baseline design. In comparison with other preliminary designs, LV for the camberline design has higher strength compared to circumferential design. The strength of LV in camberline design is reduced and it is moved closer to the SS of the blade when compared to the baseline design. Similarly, the TPV is not eliminated as in axial design but has lesser strength compared to the circumferential design. Looking at the blade tip surface, it is observed that the camberline grooves restrict the leakage flow. Near the leading edge of blade tip surface, a low momentum region for circumferential design exists which leads to reduced momentum and increased TPV strength. However, this low momentum region is not present in the case of camberline design and similar intermittent high and low shear stress zones as in axial grooves design can be observed. Beyond 30% blade chord, there are no spots of higher shear stress on the blade tip for new camberline design as compared to the axial design. Thus, there is reduced leakage flow in this region, but it is not entirely reduced as circumferential design. The circumferential grooves design has low shear stress on the blade tip, which is not the case for the new camberline design. Overall, for new design, there is a tradeoff between the leakage losses and secondary flow losses with the new, improved grooves design.

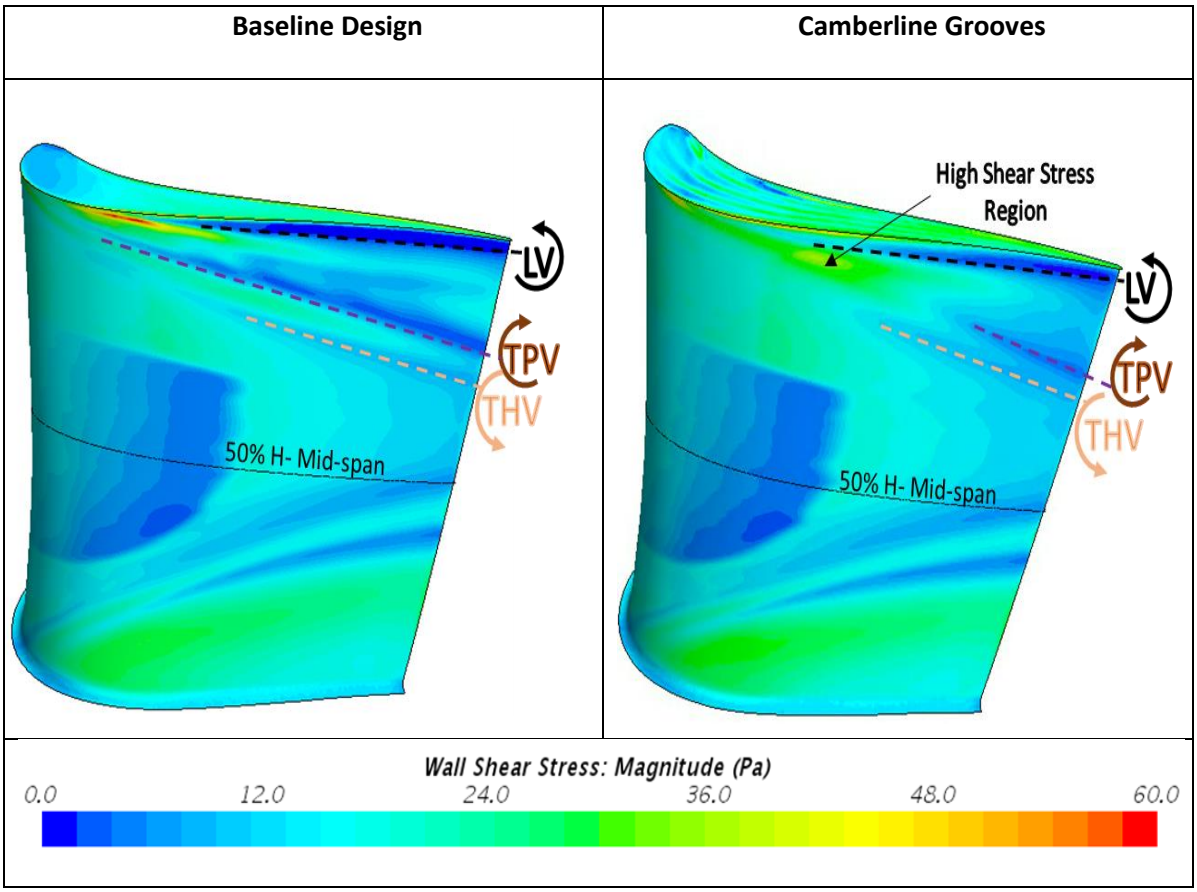


Figure 5-5 Wall Shear Stress Contour plot on the Tip Surface and Suction Side of Rotor Blade

# Chapter 6

## Summary

This thesis performed the computational simulations using the physics of the RANS technique, along with the SST k-w turbulence model. A grid dependency study was conducted to select the configuration of the optimized number of cells for the NGV and rotor sections. The mixing plane interface was instrumental in performing steady-state simulations for a stationary NGV section and rotating rotor section. The blade loading coefficient at the mid-span of NGV and rotor blade for the baseline and preliminary designs were compared to the experimental data. Further, three preliminary casing designs i.e., spherical patterns, axial grooves and circumferential grooves were introduced. The blade loading coefficients for the casing designs were similar to the baseline model in the NGV section but had minor variations in the rotor section. This was because the NGV section was unchanged for any of the designs. Pressure contour plots and other 3-D flow visualizations facilitated the understanding of vortex structures on the tip-side. The main objective of this study was to understand the complex flow characteristics in a turbine stage attributed to casing groove geometries. Tip leakage losses were discussed in depth, which formed the foundation of this study. Along with TLV, variations in TPV and THV vortex structures for each design are discussed in the results section. The FOM for each of the new designs were obtained and compared with the experimental results to assess the performance. Three preliminary casing designs analyzed were instrumental in understanding the physics of the aerodynamic losses generated in an axial turbine. The discussions on the streamwise vortical structures in the passage were useful in developing the new and improved design, which was called “Camberline Grooves Design”.

## 6.1 Conclusions

Initially, three preliminary casing designs, spherical patterns, axial grooves, and circumferential grooves, were studied. To provide a better comparison and assessment of vortex structures, delta $C_P$ plots for all of the casing designs are shown in Figure 6-1. The spherical pattern design has minor variations in comparison to the baseline design. For this design, it is observed that near 90% span the leakage vortex strength is reduced insignificantly against the baseline design due to the additional vortices generated by the presence of hemispheres. However, the TPV has gained a relatively higher strength along with a reduction of high momentum region near the tip. Thus, the performance of the spherical design is deteriorating which is indicated by a negative value of the FOM, as shown in Table 6-1.

Circumferential grooves design has the highest strength of TPV in comparison to other designs. This higher strength of TPV, however, has resulted in decreasing the strength of THV which is visible near the 75% span. However, this design has the least amount of LV strength. This type of groove orientation is optimum to reduce the momentum of leakage fluid which eliminates the LV. Below the LV section, this low momentum fluid merges with the TPV and leads to the increased strength of TPV. Thus, the positive effect created due to LV is reduced by the TPV, and hence, it has a FOM value of 3.1%, which is very low in comparison to the design of axial grooves.

Axial grooves design proved to be more efficient compared to other preliminary casing designs due to lower momentum deficit zones, which is visible in total pressure coefficient plots. Axial grooves provide an easy path for the flow to pass from PS to SS of the blade. However, due to the presence of alternating grooves and ribs generates high velocity near the casing which leads to a steeper pressure gradient. Even though the LV still exists it has a higher-pressure value in comparison to

the baseline design. In the case of LV, such orientation of grooves is although not as helpful as circumferential grooves design, but it has a significant effect on the TPV elimination. As noticed, the highest delta $C_P$ values for the axial case occurs near 85% span where secondary losses by the TPV are reduced for this design. However, secondary losses generated by the THV increases which can be attributed to the absence of counter-rotating TPV. These adverse effects produced by THV are seen below the 80% span. As a result, along with LV, there is a need to consider secondary losses generated due to leakage flow.

The flow physics study for axial and circumferential grooves design lead to the design of camberline grooves. The grooves profile for camberline design is a blend of both the designs. The LV for the camberline design is not eliminated significantly as compared to circumferential design but it has higher pressure gradient values which is helpful for the delta $C_p$ values. The new design has a high momentum region similar to the axial case, which is absent in the circumferential case. The TPV is present as well in the camberline design, unlike an axial case, which puts a check on the strength of secondary flows below it. However, the TPV of camberline design has reduced strength in comparison to the circumferential design as it does not reduce the momentum of the fluid to a low level. Overall, it provides better benefits than other casing designs as it has the best FOM value of 30.7%.

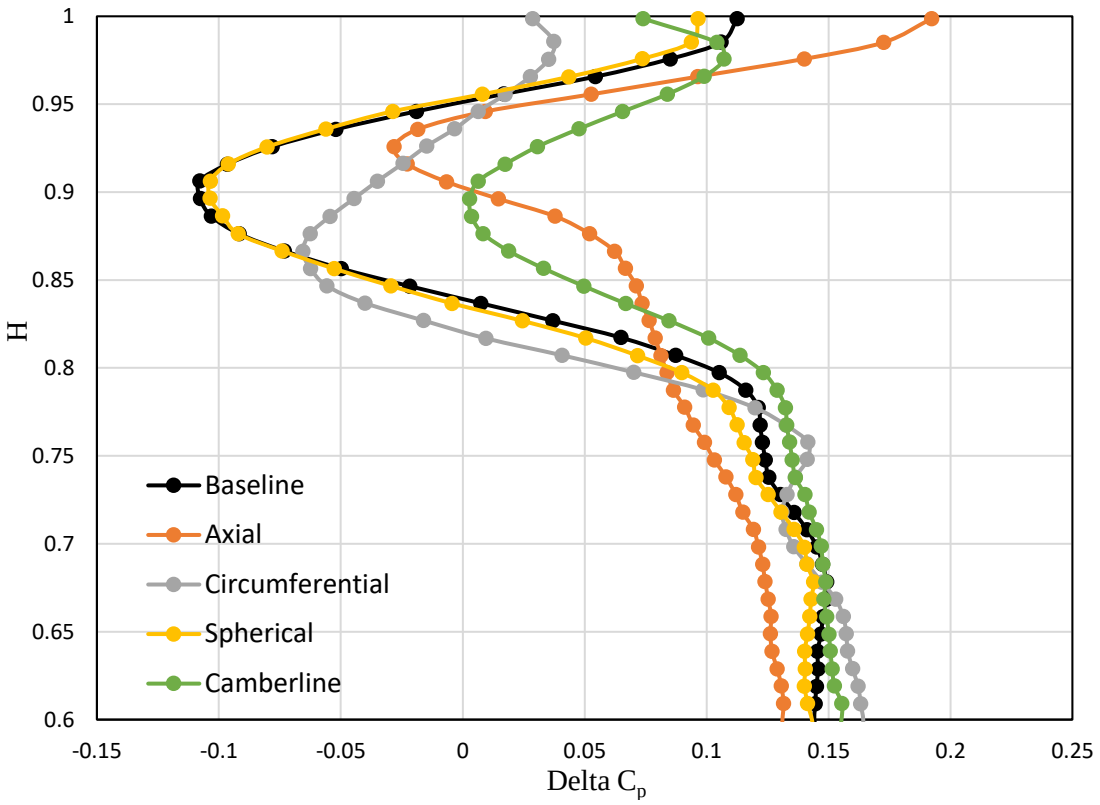


Figure 6-1 Delta $C_P$ Plot for all the Casing Designs in Comparison with the Baseline Design.

Table 6-1 Performance Summary: Table of FOM

| **Design** | **Tip_FOM (70 to 97% H)** | |
|---|---|---|
| | **Experimental** | **CFD** |
| Spherical Patterns | -3.7 % | -3.6 % |
| Axial Grooves | 19.4 % | 20.8 % |
| Circumferential Grooves | 3.9 % | 3.1 % |
| Camberline Grooves | - | 30.7 % |

## 6.2 Future Scope

Based on the observations from the current computational effort, a few modifications are suggested for possible improvements in the turbine stage performance. Optimization of grooves design, particularly the orientation of the grooves in proper angle and their dimensions, can be varied to improve overall efficiency. The camberline design was one of the improved designs. However, by using different optimizations algorithms, the most optimal casing design for the current system can be found. An unsteady flow study can be implemented using U-RANS and harmonic balance technique to study the flow details inside the grooves.

A realistic engine model's boundary conditions could be utilized to study the effects of the grooves. The efficiency of the high-speed realistic engine can be accurately determined as against the low-speed cold flow facility of AFTRF. Dissipation function variations can be utilized in locating the total high-temperature regions. Eventually, casing grooves can be proven useful for turbine cooling research based on the enthalpy calculations. Finally, the current simulations should also account for isothermal boundary conditions instead of the current adiabatic wall boundary conditions. This would help to obtain accurate data for the engines with very high exit temperatures.

# Appendix

## A-1 AFTRF Schematic

Figure A- 1 provides the detailed dimensions of the AFTRF. The CAD model for the analysis was developed based on these dimensions.

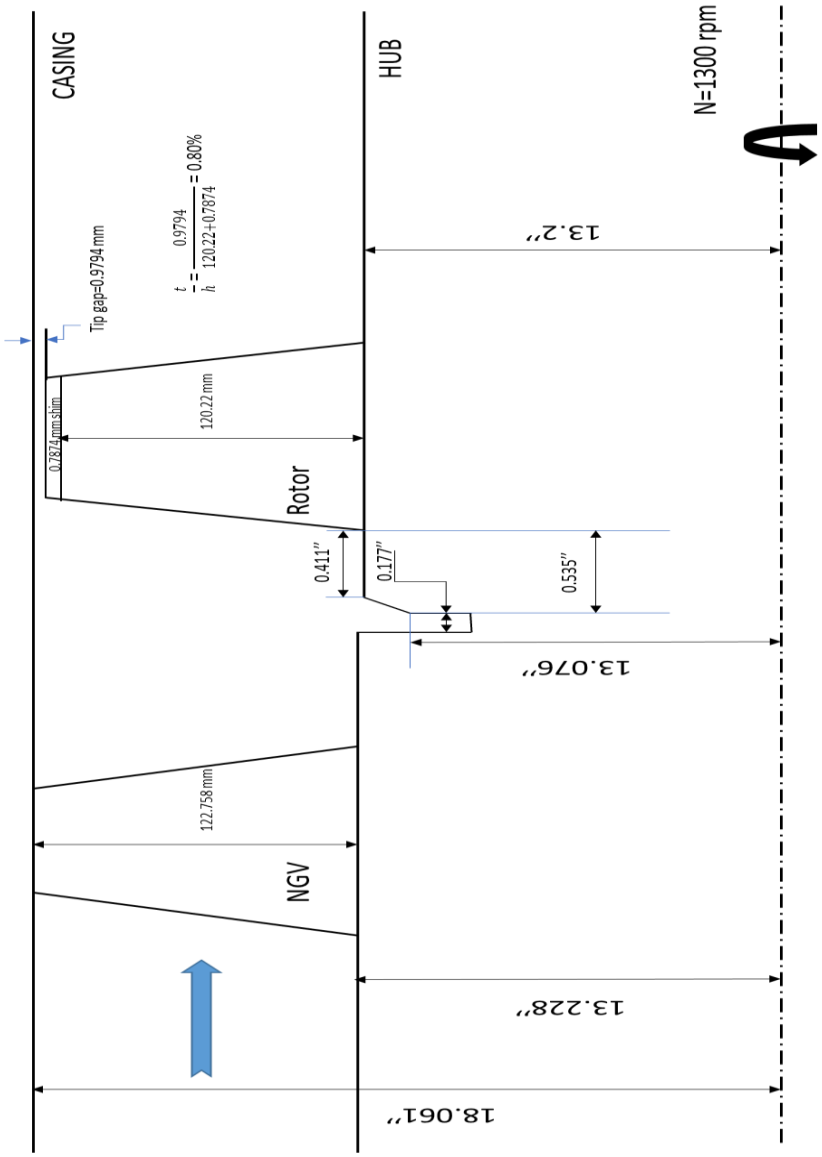


Figure A- 1 Detailed schematic of AFTRF [15]

**A-2 Efficiency Study for AFTRF Facility and Realistic Engine Conditions**

This part of the appendix discusses why the total pressure data is utilized for the calculation of performance of the turbine stage in AFTRF and not the total to total turbine efficiency of the stage. It eventually leads to the acceptance of the fact that the total to total efficiency measurements in AFTRF is not reasonably accurate based on its operating conditions.

The case study for AFTRF efficiency explained in this section is based on the explanation of Doshi [15]. The total-to-total isentropic efficiency is given as the ratio of the actual change in stagnation enthalpy to the theoretical (isentropic) change in enthalpy. This efficiency calculation is done using Equation A-1.

$$\eta_{T\,T} = \frac{h_{01} - h_{03}}{h_{01} - h_{0m\,s}} = \frac{1 - \frac{T_{03}}{T_{01}}}{1 - \left(\frac{P_{03}}{P_{01}}\right)^{\frac{\gamma-1}{\gamma}}}$$

.....Equation A- 1

Equation A-1 explains that efficiency is a function of total temperature and total pressure ratios. Subscript “01” designates the NGV inlet conditions, and the subscript “03” represents the stage exit conditions. Total-to-total efficiency is strongly dependent on the total temperature ratio. This is especially true for low-speed turbine operation that is the case for the AFTRF. This dependency is much less significant for a turbine stage operating under field-realistic conditions. This is proved by the sensitivity analysis.

For the sensitivity analysis of efficiency dependency, the change in efficiency values ($\delta\eta_{TT}$) were compared for AFTRF, a low-speed turbine ($P_{o3}/P_{o1}$=0.94), with the realistic engine conditions ($P_{o3}/P_{o1}$=0.5). Equation A-2 was used to calculate the change in the efficiency. The efficiency change is based on change in temperature and pressure at the exit which is shown in equations A-3 and A-4 respectively. For the AFTRF, the inlet pressure ($P_{o1}$) is 101338 Pa and inlet temperature

($T_{o1}$) is 289 K. While, for the case of realistic engine, combustion outlet temperature and pressure are very high. Based on the present turbine stage data, the inlet pressure ($P_{o1}$) and inlet temperature ($T_{o1}$) was selected as 10600 kPa is 1900 K respectively for the realistic engine. For the current analysis, the variations of pressure ($\delta P_{o3}$) and temperature ($\delta T_{o3}$) of 100 pa and 2 K respectively. It was proven from the study, shown in Figure A- 3, that if there is a change of stage exit total temperature by about 0.5 K, then the total-to-total isentropic efficiency of AFTRF turbine stage will be easily changed by about 10%. The total-to-total efficiency may easily vary more than 30% if the low-speed turbine (AFTRF) operator assumes a $\pm 2\ K$ variation (error) at the stage exit. Whereas for realistic engine case, a $\pm 2\ K$ variation (error) at the stage exit produces just 0.6% variation in efficiency. The strong dependency of efficiency to $\delta T_{03}$ for AFTRF is shown in Figure A- 3 and A-3. The dependency of efficiency to $\delta P_{03}$ is much less significant for both the cases.

$$\delta\eta_{TT} = \sqrt{\left[\frac{\partial\eta_{TT}}{\partial T_{03}}\delta T_{03}\right]^2 + \left[\frac{\partial\eta_{TT}}{\partial P_{03}}\delta P_{03}\right]^2}$$

.....Equation A- 2

$$\frac{\partial\eta_{TT}}{\partial T_{03}} = -\frac{1}{T_{01}\cdot\left[1-\left(\frac{P_{03}}{P_{01}}\right)^{\frac{\gamma-1}{\gamma}}\right]}$$

.....Equation A- 3

$$\frac{\partial\eta_{TT}}{\partial P_{03}} = \frac{\frac{\gamma-1}{\gamma}\cdot\left(\frac{P_{03}}{P_{01}}\right)^{\frac{-1}{\gamma}}\cdot\left(1-\frac{T_{03}}{T_{01}}\right)}{\left[1-\left(\frac{P_{03}}{P_{01}}\right)^{\frac{\gamma-1}{\gamma}}\right]^2}$$

.....Equation A- 4

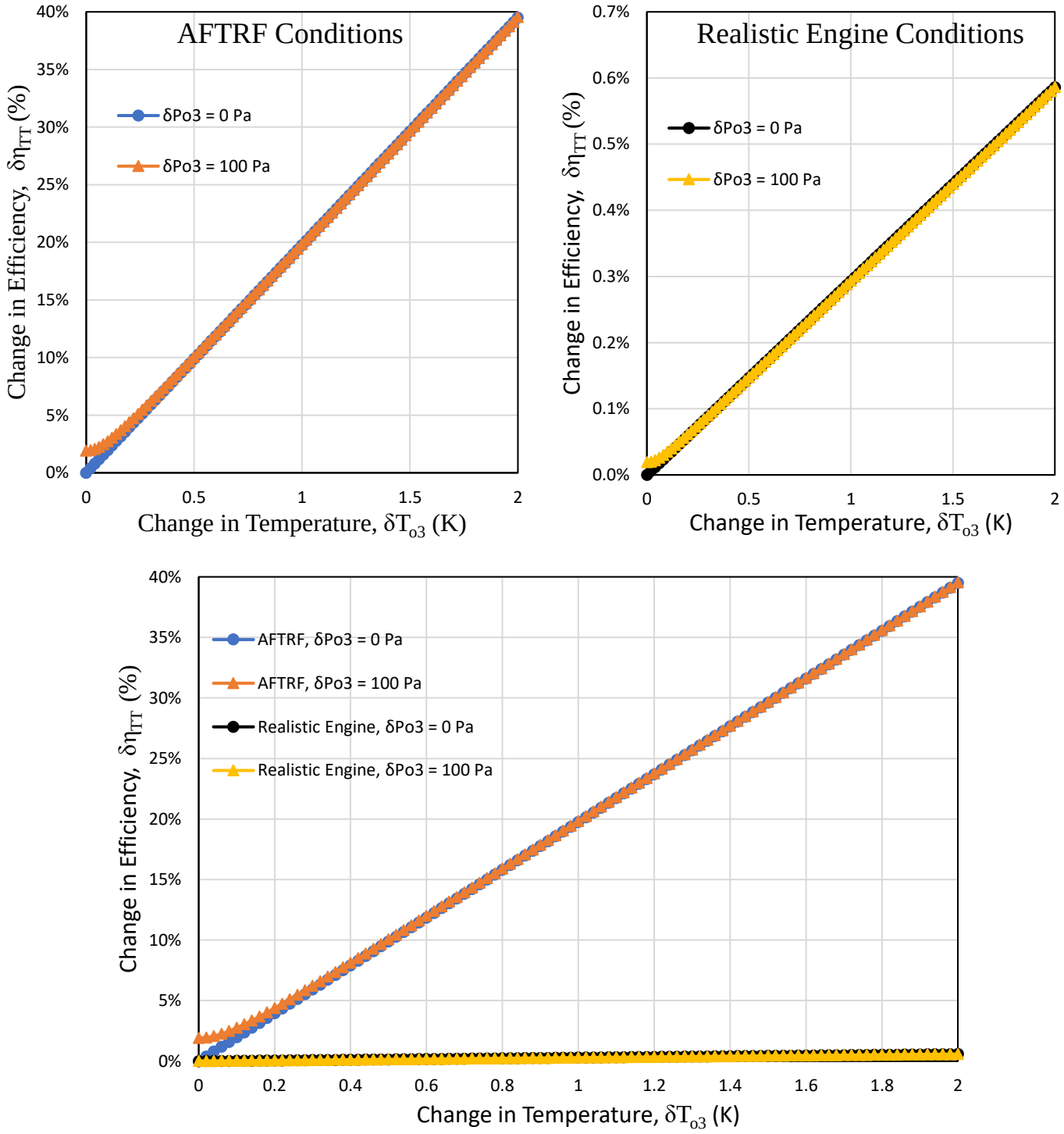


Figure A- 2 Change in Efficiency with Respect to Change in Temperature for AFTRF (top-left), Realistic Engine Conditions (top-right) and for Both (on the same scale)

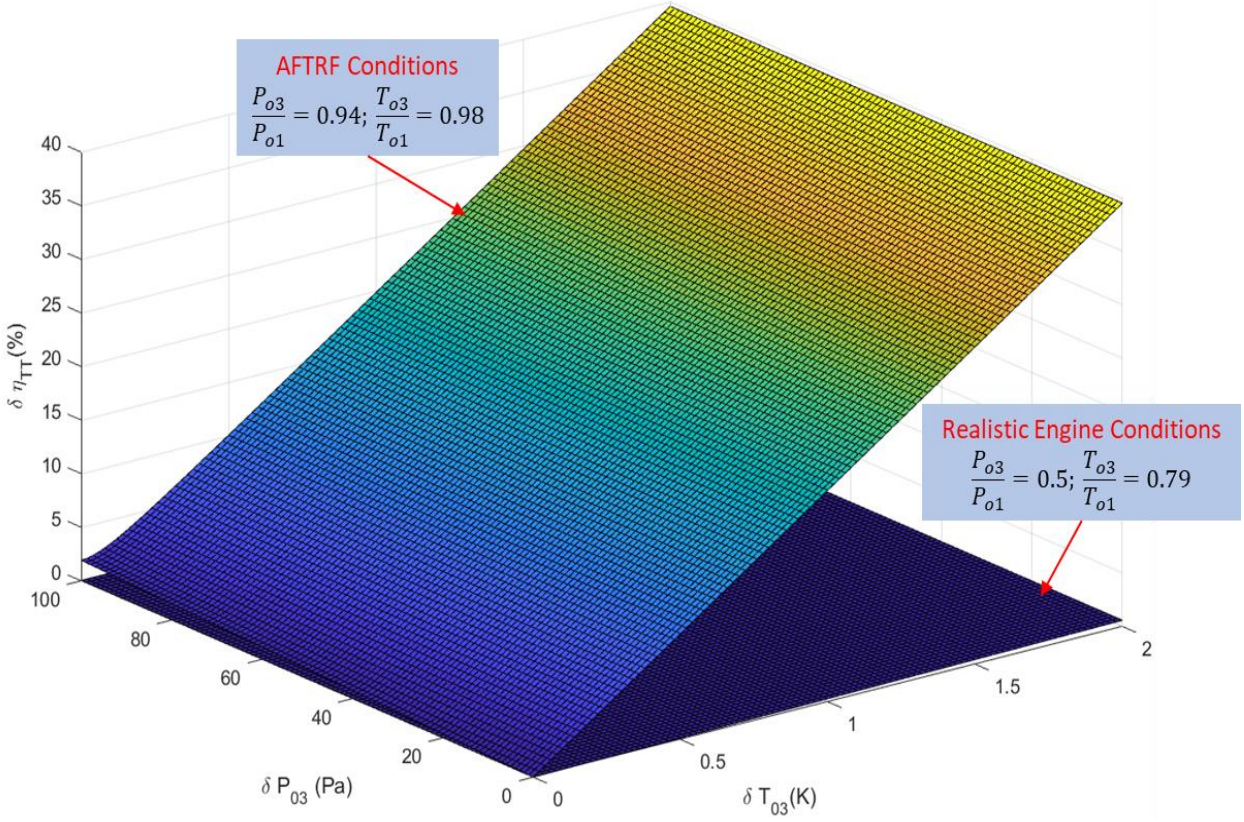


Figure A- 3 Sensitivity Analysis of Efficiency with Respect to Pressure and Temperature [15]

So, the sensitivity of a realistic engine's efficiency to exit total temperature and pressure is not as strong as that of the AFTRF in low-speed operation with a small pressure drop throughout the stage. In addition, AFTRF stage total temperature drop is only 4 to 5 K, so it is possible that the total to total efficiency calculation has a huge error. Because of all these difficulties in generating AFTRF total-to-total efficiency (experimentally and computationally), a Figure of Merit (FOM) based on phase-locked total pressure measurements was used for turbine performance assessment. Assessments based on the total-to-total efficiency were not established because of inherent errors in quantifying total-to-total efficiency.

In total-to-total efficiency calculation for this CFD study, outlet will be considered as a measurement plane in order to have a comparison with FOM values on that plane. The measurement plane is at 25.4 mm from the rotor trailing edge. From Figure A- 4 shown below, the temperature variation at the measurement plane is less than 2 K for all the casing designs. The curves in efficiency plots look just opposite to the temperature plots. As discussed, the temperature variations play a higher role in the efficiency calculations. With present day temperature sensing devices, the temperatures at such cold flow facility cannot be predicted with very high accuracy.

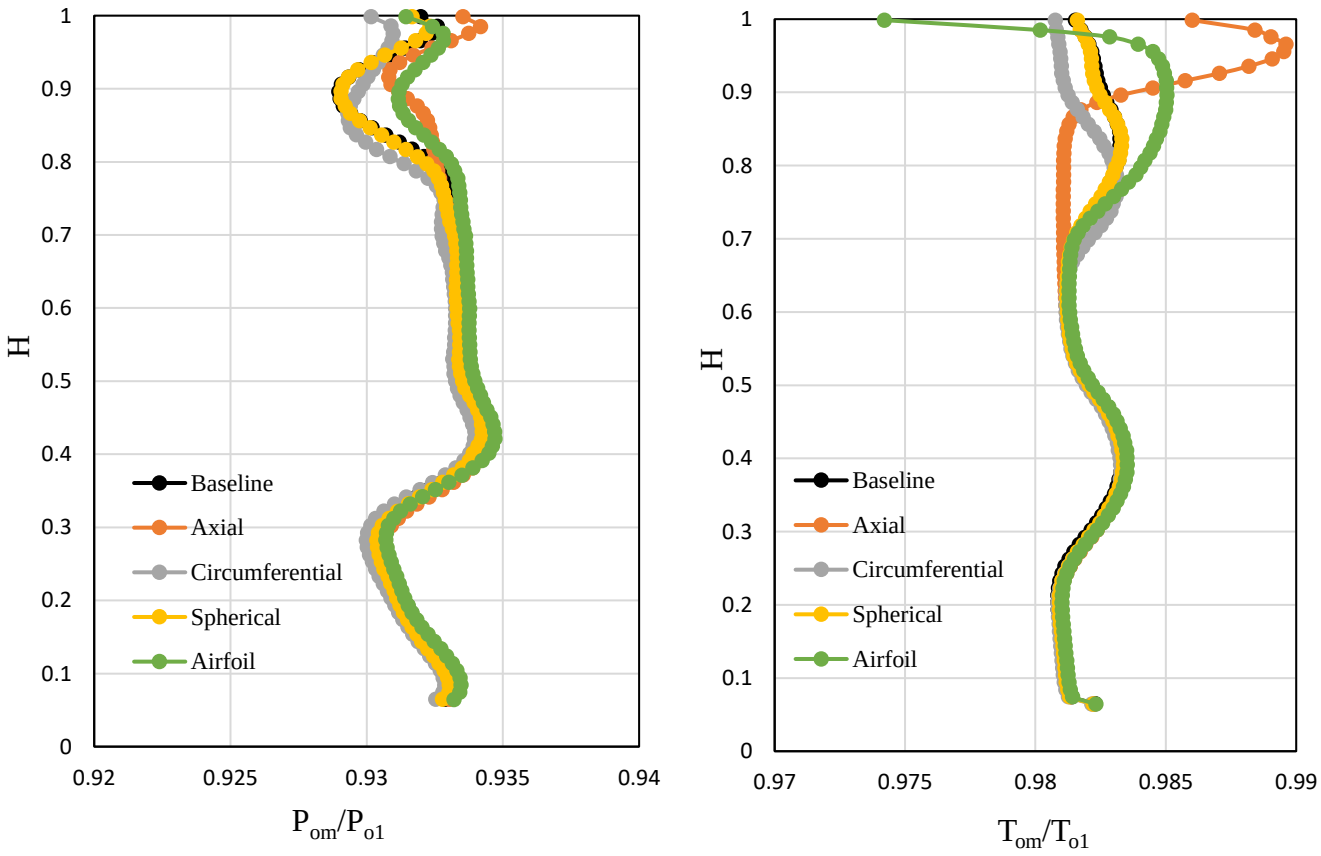


Figure A- 4 Spanwise Distribution for all the Casing Designs

Pressure Ratio (Top-left); Temperature Ratio (Top-right)

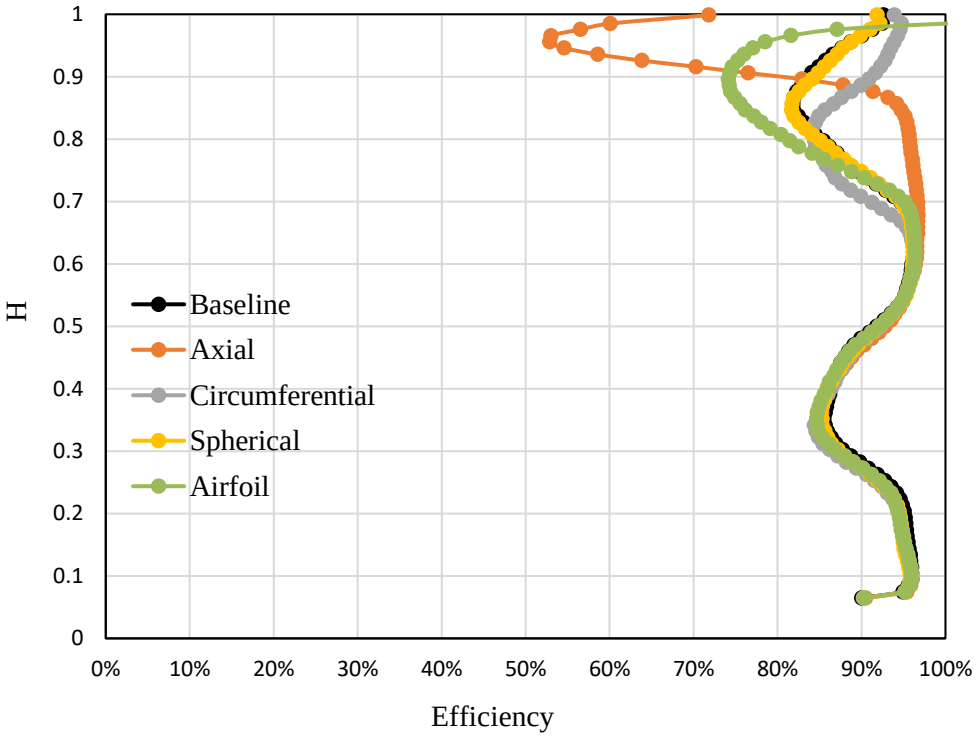


Figure A- 5 Spanwise Distribution of Efficiency for all the Casing Designs

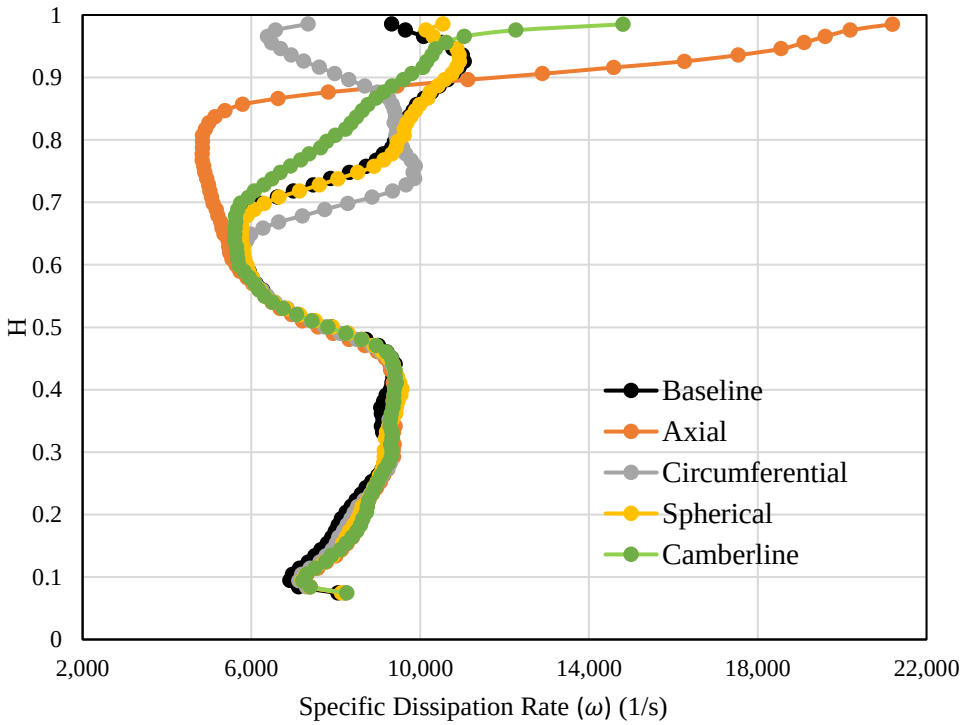


Figure A- 6 Spanwise Distribution of Specific Disssipation Rate for all the Casing Designs

The specific dissipation rate is the rate in which useful turbulent kinetic energy and mean flow to motion is converted into non-useful, internal energy of the fluid. It means wastage of useful energy in heating up the fluid. In turbulent flow, specific turbulence dissipation rate(w) is usually dominating. Viscous dissipation is very high in regions of high gradients like boundary layers, shear layers, etc. and in high turbulence regions like in wakes and vortices. This leads to substantial rise in temperature near the boundary layers, in secondary flows, tip vortices or wakes, due to viscous dissipation. The viscous dissipation term involves a second order of shear strain rate. This means a slight variation of the velocity in space may result in a very high variation of viscous dissipation term. Eventually resulting in errors in temperature predictions for such low-temperature facilities.

# Bibliography

[1] Lakshminarayana, B., 1995, “Fluid Dynamics and Heat Transfer of Turbomachinery”, John Wiley & Sons Inc; 1st Edition.

[2] Mattingly, J.D., 2006, “Elements of propulsion: gas turbines and rockets”, AIAA Education Series, American Institute of Aeronautics and Astronautics.

[3] Langston, L.S., 2001, “Secondary Flows in Axial Turbines – A Review”, Heat Transfer in Gas Turbine Systems, Annals of the New York Academy of Sciences.

[4] Sharma, O. and Buttler, T., 1987, “Predictions of Endwall Losses and Secondary Flows in Axial Flow Turbine Cascades”, Journal of Turbomachinery. ASME Paper No. 86-GT-228.

[5] Beristain, I., 2012, “Aerodynamic Analysis of Axial Fan Unsteady Simulations”, Master’s Thesis, University of Basque Country.

[6] Sieverding, C. H., and Van den Bosche, P., 1983. “The use of Coloured Smoke to Visualize Secondary Flows in a Turbine-Blade Cascade”, Journal of Fluid Mechanics.

[7] Boyle, R. J., Haas, J. E., Katsanis, T., 1984, “Comparison between Measured Turbine Stage Performance and the Predicted Performance using Quasi-3D Flow and Boundary Layer Analyses,” NASA TM-83640, presented at the 20th AIAA/ASME/SAE Joint Prop. Conf.

[8] Andichamy, V. C., Khokhar, G. T., Camci, C., 2018. “An Experimental Study of using Vortex Generators as Tip Leakage”, ASME Turbo Expo.

[9] Gumusel, B., 2008, “Aerodynamic and Heat Transfer Aspects of Tip and Casing Treatments used for Turbine Tip Leakage Control”, Doctoral Thesis, Pennsylvania State University.

[10] Rao, N., Gumusel, B., Kavurmacioglu, L., Camci, C., 2006, “Influence of Casing Roughness on the Aerodynamic Structure of Tip Vortices in an Axial Flow Turbine”, ASME Turbo Expo 2006.

[11] Kavurmacioglu, L., Senel, C.B., Maral, H., Camci C., 2018, "Casing Grooves to Improve Aerodynamic Performance of a HP Turbine Blade", Aerospace Science and Technology.

[12] Lakshminarayana, B., Camci, C., Halliwell, I., Zaccaria, M., 1996, "Design, Development, and Prediction of a Turbine Research Facility to Study Rotor Stator Interaction Effects", Int. Journal of Turbo and Jet Engines.

[13] Camci, C., 2004, "A Turbine Research Facility to Study Tip Desensitization Including Cooling Flows", VKI Lecture Series on "Turbine Blade Tip Design and Tip Clearance Treatment".

[14] STAR CCM+, 12.02.011-R8 User Manual: http://www.cd-adapco.com/products/star-ccm/documentation

[15] Doshi, M., 2018, "Computational Prediction of a Large-Scale HP Turbine Flow against Measured Aerodynamic Data", Master's Thesis, The Pennsylvania State University, December 2018.

[16] Zaccaria, M., 1994, "An Experimental Investigation into the Steady and Unsteady Flow Field in an Axial Flow Turbine", Doctoral Thesis, Pennsylvania State University.

[17] Averbach M., 2014, "Simulation and Experimental Validation of the Wheel Space of the Axial Flow Turbine Research Facility Under Low Purge Flow Conditions", Master's Thesis, Pennsylvania State University.

[18] Menter, F.R, 1994, "Two-equation Eddy-Viscosity Turbulence Modeling for Engineering Applications", AIAA Journal.

[19] Maral, H., Senel, C.B., Kavurmacioglu, L., Camci, C., 2016, "Aerothermal Performance of Partial and Cavity Type Squealer Tip in a Linear Cascade", Journal of Thermal Engineering.

[20] Town, J., Akturk, A., Camci, C., 2012, "Total Pressure Correction of a Sub-Miniature Five-Hole Probe in Areas of Pressure Gradients", ASME Paper No. GT2012-69280.

[21] Town, J., 2012, “An Automated Calibration and a Correction Scheme for Total Pressure Gradient Effects of Subminiature Five-Hole Probe”, Master’s Thesis, Pennsylvania State University.

[22] Rolfes, M., Lange, M., Vogeler, K., Maliach, R., 2017, “Experimental and Numerical Investigation of a Circumferential Groove Casing Treatment in a Low Speed Axial Research Compressor at different Tip Clearances”, ASME Turbo Expo.

[23] Kawase, M., Rona, A., 2019, “Effect of a Recirculating Type Casing Treatment on a Highly Loaded Axial Compressor Rotor”, International Journal of Propulsion and Power.

[24] Dey, D., 2001, “Aerodynamic Tip Desensitization in Axial Flow Turbines”, Doctoral Thesis, Pennsylvania State University.

[25] Chernobrovkin, A., 1999, “Numerical Simulation of Complex Turbomachinery Flows”, Doctoral Thesis, Pennsylvania State University.

[26] Andichamy, V. C., Camci, C., Kim, Y.W., 2019. “An Experimental Study of Passage-to-Passage Flow Interactions in a Single Stage Axial Flow Research Turbine Rotor”, ASME Turbo Expo.